nature nanotechnology

Review article

https://doi.org/10.1038/s41565-023-01354-x

Layered materials as a platform for quantum technologies

Received: 19 August 2022

Accepted: 17 February 2023

Published online: 15 June 2023

Check for updates

Alejandro R.-P. Montblanch[1,5], Matteo Barbone[1,2,6,7], Igor Aharonovich[3,4], Mete Atatüre[1] & Andrea C. Ferrari[2]

Layered materials are taking centre stage in the ever-increasing research effort to develop material platforms for quantum technologies. We are at the dawn of the era of layered quantum materials. Their optical, electronic, magnetic, thermal and mechanical properties make them attractive for most aspects of this global pursuit. Layered materials have already shown potential as scalable components, including quantum light sources, photon detectors and nanoscale sensors, and have enabled research of new phases of matter within the broader field of quantum simulations. In this Review we discuss opportunities and challenges faced by layered materials within the landscape of material platforms for quantum technologies. In particular, we focus on applications that rely on light–matter interfaces.

Quantum technologies (QTs) target applications that go beyond their classical counterparts by exploiting the quantum properties of particles for the processing and transfer of information[1]. The fundamental building blocks that enable quantum computing, communications, networks, simulations and sensing are known as qubits[1]. Optically active qubits (Box 1) are of particular interest because they allow for direct interfacing between stationary qubits and flying qubits, essential for the transmission of quantum information. The development of atomic systems operating as optically active qubits, such as trapped ions[1] and lattices of Rydberg atoms[2], has led to the commercialization of quantum processor architectures for noisy intermediate-scale quantum computation (for trapped ions, see, for example, companies such as Oxford Ionics, Alpine Quantum Technologies, Quantinuum or IonQ; for Rydberg atoms, see, for example, companies such as QuEra or PASQAL). Architectures using flying qubits in linear-optical quantum computing (LOQC)[1] have already shown quantum advantage by using boson sampling on an optical bench[3], while on-chip LOQC platforms are being explored for commercialization (for LOQC, see, for example, the company PsiQuantum). Challenges common to all these approaches include scalability and operational complexity. Alternatively, optically active spin qubits in solids offer the opportunity of direct on-chip integration and no overhead of infrastructure for trapping schemes. This imposes more stringent fabrication conditions to meet the requirements for photon indistinguishability, high zero-phonon line (ZPL) emission and long spin coherence times T_2 (Box 1). Multiple light-interfaced solid-state platforms have been investigated over the past 30 years[4], including semiconductor quantum dots (QDs)[5–7] (Supplementary Tables 1 and 2), atomic defects in diamond[8–10] (Supplementary Tables 3 and 4), Si[11–13], SiC[14–16] (Supplementary Tables 5 and 6), rare-earth ions[17–19] (Supplementary Tables 7 and 8) and nanotubes[20,21].

Optically active qubits for on-chip, photonic QTs should be scalable, with deterministic generation on pre-specified locations, should be integrable with photonic structures and allow for all-electrical control. Layered materials (LMs)[22] are emerging as a new platform capable of meeting these QT requirements: we are at the dawn of the era of layered quantum materials.

LMs are solids with highly anisotropic bonding, constituted by internally strongly bonded sheets, weakly bonded to adjacent layers[22]. Each individual sheet within a LM, called a monolayer (1L), is formed by atoms covalently bonded together. There are over 5,000 LMs[23,24], with at least 1,800 that are exfoliable[23]. Only a small fraction of these have so far been experimentally investigated, including graphene,

[1]Cavendish Laboratory, University of Cambridge, Cambridge, UK. [2]Cambridge Graphene Centre, University of Cambridge, Cambridge, UK. [3]School of Mathematical and Physical Sciences, University of Technology Sydney, Ultimo, New South Wales, Sydney, Australia. [4]Australian Research Council Centre of Excellence for Transformative Meta-Optical Systems, University of Technology Sydney, Ultimo, New South Wales, Sydney, Australia. [5]Present address: QuTech and Kavli Institute of Nanoscience, Delft University of Technology, Delft, The Netherlands. [6]Present address: Munich Center for Quantum Science and Technology, (MCQST), Munich, Germany. [7]Present address: Walter Schottky Institut and Department of Electrical and Computer Engineering, Technische Universität München, Garching, Germany. e-mail: ma424@cam.ac.uk; acf26@eng.cam.ac.uk

https://doi.org/10.1038/s41565-023-01354-x

BOX 1

Quantum technologies with optically active spin qubits

A qubit is a quantum two-level system with two distinct, well defined, isolated and accessible energy levels, each associated with a different quantum state, typically labelled $|0\rangle$ and $|1\rangle$ (ref. 204). In contrast to a classical bit, which can only be in one specific state at a time, 0 or 1, a qubit can be in any superposition of $|0\rangle$ and $|1\rangle$ (ref. 204). As such, the state $|\psi\rangle$ representing the wavefunction of a qubit is expressed as[204] $|\psi\rangle=\alpha|0\rangle+\beta|1\rangle$, with α and β complex coefficients, which store the information and obey the normalization relation $|\alpha|^2+|\beta|^2=1$ (ref. 204). This allows for a quantum register size (i.e. the number of configurations stored at the same time) that scales as 2^N, with N the number of qubits[204]. This is in contrast with the linear scaling for classical bits.

Storage and manipulation of quantum information is primarily achieved using matter-based stationary qubits, or qubits fixed in space. Implementations of stationary qubits include neutral atoms, electrostatically trapped ions, superconducting qubits, and spins in solids[1]. Transferring quantum information over long distances relies typically on single photons in the optical and NIR domains acting as flying qubits[1]. Therefore, interfacing flying and stationary qubits, or light and matter, efficiently is an overarching challenge for multisystem interconnectivity. This can be done indirectly by using transducers, which have already achieved conversion between microwave and optical parts of the electromagnetic spectrum at single-quantum level[138]. Some qubit candidates offer direct optical access and a natural interface to single photons without a finite-efficiency conversion step. Qubits that meet this requirement are called optically active qubits, and include trapped ions[205], single molecules[206], neutral atoms, semiconductor QDs[4], and atomic defects in wide-bandgap materials, such as diamond or SiC[4] (see figure in this box). The deployment of transmission lines kept at dilution refrigerator temperature has extended the spectrum for quantum information transfer to include microwave photons[207].

The ability of optically active qubits to emit single photons, or antibunched light, is measured by the single-photon purity[29], or the photon–photon correlation function $g^2(\tau)$ at a delay time $\tau=0$, $g^2(0)$. Ideally, the probability of emitting more than one photon at the same time is zero, $g^2(0)=0$. Single-photon emission is verified when $g^2(0)<0.5$. A saturating emission as a function of the laser power used to pump the emitter is one indication of single-photon emission. The speed of the optical processes to be performed with the emitted photons can be enhanced by improving the ability to collect photons (called photon-extraction efficiency), by reducing the time the emitter spends in an optically excited quantum state (called excited-state lifetime) or by improving the ability of the emitter to transform input energy quanta into photons (called quantum efficiency). Quantum communication protocols depend critically on source brightness, single-photon purity, stability and wavelength. However, they do not necessarily demand the emission of coherent photons. This is an additional requirement for the generation of quantum-entangled states between remote emitters, the basis of quantum networks. A quantum-entangled state, or entangled state, is a quantum state between two qubits that cannot be factorized, thus the quantum information is shared between the two[204]. Coherent photons are emitted into the ZPL of the emission spectrum of an emitter and do not involve any Stokes or anti-Stokes process, the latter two constituting the phonon sideband of an emitter. The Debye–Waller factor is the ratio of ZPL photons to total emitted photons, and is ideally close to unity. Photon indistinguishability[29,208] for the generation of entangled states requires the reliable generation of ZPL photons with transform-limited linewidth, identical emission energy and well-defined polarization. The indistinguishability of photons is measured using a Hong–Ou–Mandel experiment.

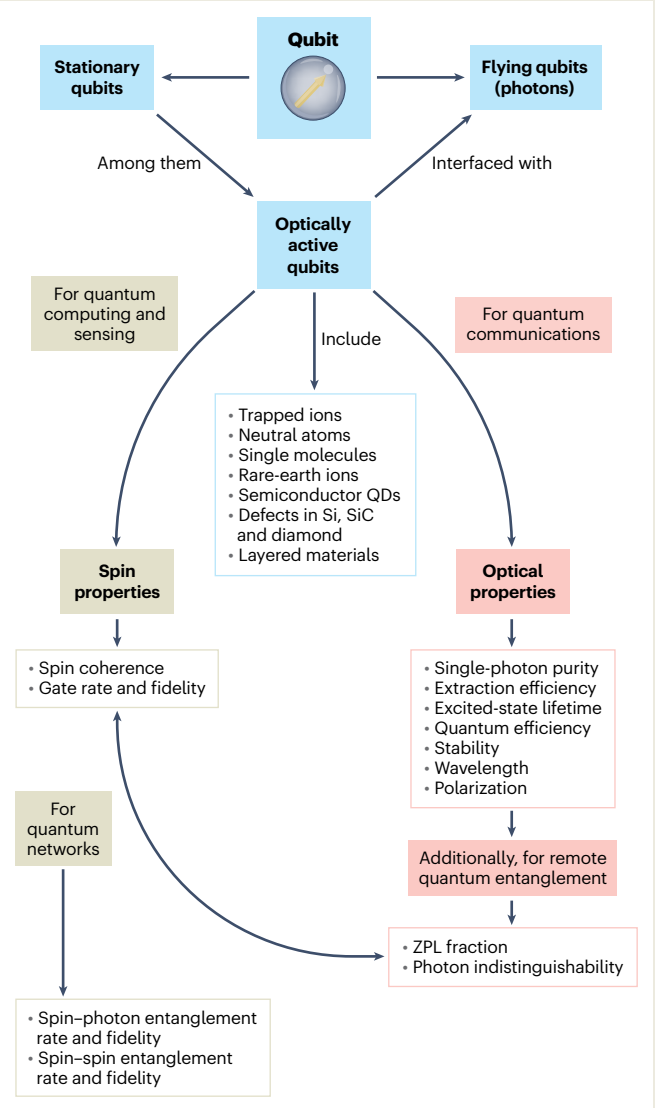

Optically active qubits that use spin quantum states to encode and process quantum information are known as optically active spin qubits. The quantum state of a spin in an optically active spin qubit is typically coherently manipulated using microwaves. In the simplest experiments, the time that quantum information can be stored in a spin before randomized interactions with the environment lead to its degradation, is denoted T_2^*. This can be extended by applying additional microwave pulses to decouple the spin from the environment[209] to reach the coherence time of the spin, T_2. A long enough T_2 benchmarks the ability to perform multiple consecutive quantum operations, especially relevant if the spin is acting as a quantum memory. Sources of decoherence typically include coupling to a fluctuating nuclear-spin bath or lattice phonons. Improving the speed and correctness (or fidelity) with which quantum

(continued from previous page)

logic gates are applied to the spin in quantum information protocols is key for quantum networks and computing[204].

Entanglement between a matter qubit and a photon allows quantum information to transfer from the matter to a flying qubit, travel and link to other qubits. This forms the quantum link between stationary and flying qubits[4], and with logic operations and optical communications[4]. Ideally, both generation rate and fidelity of spin–photon entangled states should be high, as in many cases the generation rate and fidelity of spin–spin entangled states between remote optically active spin qubits depend on the former.

hexagonal boron nitride (hBN), black phosphorus, transition-metal dichalcogenides (TMDs), III-metal monochalcogenides and MXenes[22]. LMs encompass superconductors, topological insulators, conductors, piezoelectric and ferroelectric materials[22,25], among others. TMDs such as WSe_2, WS_2, $MoSe_2$, MoS_2, WTe_2 or $MoTe_2$ are direct-bandgap semiconductors in the 1L limit[26], while 1L-hBN remains an insulator with an indirect gap ~6 eV (ref. 27).

1Ls can be isolated by mechanical exfoliation from bulk crystals[22,28], ideal for proof-of-concept devices. Chemical-vapour deposition, metal–organic chemical-vapour deposition, molecular beam epitaxy or other techniques have been used for wafer-scale growth[22,28].

The potential applications of LMs cover all areas of QTs, as showcased in Fig. 1. Some LMs, including TMDs and hBN, host single-photon emitters (SPEs)[29], discrete-energy systems that emit one single photon at a time, with potential for applications in quantum communications.

LMs as SPE hosts are promising for QTs due to their strong light–matter interaction[26], critical for efficient photon–qubit coupling; their atomic-scale thickness, leading to a higher photon-extraction efficiency than in non-LM systems[30] and easier integration with photonic[31] and plasmonic[32,33] devices; wafer-scale fabrication[22,28]; and tunability offered by stacking different LMs on top of one another to form LM heterostructures (LMHs) with on-demand functionality[22,28].

Endowing these SPEs with a spin promotes them to optically active spin qubits for quantum networks or computing. In quantum simulations, the superlattices generated by stacking two 1L-TMDs can be used as solid-state alternatives to artificial optical lattices[34]. 1L-TMDs and hBN could be used as novel magnetic sensors by taking advantage of the optical selection rules[35], or applying optically detected magnetic resonance (ODMR)[36]. Graphene structures can be used as on-chip-integrated near-infrared (NIR) single-photon detectors (SPDs)[37].

Here, we assess LMs as a QT platform. The wide variety of technological applications, reduced dimensionality, stability and ease of access to integrated devices make LMs an ideal platform for optics-based, solid-state implementations of QTs. We review recent progress, pinpoint outstanding challenges and discuss opportunities. We then highlight the application domains where LMs offer promise in terms of both improved performance and new operational modalities. We conclude by highlighting the areas where more research is necessary to develop this nascent technology to maturity.

Building blocks of quantum technologies with layered materials

SPEs in LMs were first investigated for QT applications[38–42], and constitute a large portion of current LM QT research. Hence, this section focuses mainly on SPEs in LMs.

The variety of available LMs[23] implies a variety of potential SPE material hosts. SPEs are found in semiconductor TMDs WSe_2[38–42], WS_2[43], $MoSe_2$[44], MoS_2[45] and $MoTe_2$[46] (Supplementary Table 9). As in diamond impurities, defects in hBN can emit single photons[47] (Supplementary Tables 10 and 12). The assembly of LMs in LMHs has led to the creation of localized dipolar excitons[48–51] in type-II LMHs (Fig. 2), including via moiré superlattices[52] (Supplementary Table 11). SPEs and saturating emission are also observed in III-metal monochalcogenides, such as GaSe[31,53] and InSe[54] (Supplementary Table 9), and in 1L-Janus WSeS[55] (Supplementary Table 9).

WSe_2 and other transition-metal dichalcogenides

WSe_2 is the most widely studied TMD host for SPEs, primarily in its 1L form, although SPEs can also be found in multilayer (ML) WSe_2[39]. 1L-WSe_2 SPEs typically emerge at cryogenic temperatures[38–42], but can be observed up to 150 K (refs. 56,57). They are commonly found between 1.51 and 1.71 eV, below the optical bandgap of 1L-WSe_2. Typical single-photon purity is ~0.1 (ref. 58), but can be as low as ~0.022 (ref. 59). SPEs in 1L-WSe_2 usually show orthogonal-linearly polarized[38,42] fine-structure splitting of the order of hundreds μeV[42], due to electron–hole exchange interaction. Their response to an external magnetic field is stronger than that of free excitons[60,61], with a g factor of the order of 9 (refs. 39–42).

Deterministic and large-scale generation of SPEs in 1L-TMD can be achieved using a nanopillar-patterned substrate[58,62] (Fig. 3a,c), where the position accuracy is defined by the nanopillar diameter (typically <100 nm)[58,62]. At each nanopillar location, the 1L-TMD conforms to the substrate and exciton localization takes place. This results in SPE occurrence probability close to 100% (refs. 58,62). By increasing the nanopillar height to ~190 nm, the probability of only a single SPE in a nanopillar site is ~90% (ref. 58). Other strategies to generate SPEs on demand include the use of Au nanocubes[63], or nanoindentation[64] (Fig. 3a).

Coupling SPEs to cavities[63,65] or plasmonic structures[32,66] can enhance emission rate, and reduce linewidth and background emission via the Purcell effect. Au plasmonic cavities have raised the emission rate of deterministically created SPEs in 1L-WSe_2 to ~42 MHz (ref. 63) by reducing the lifetime to hundreds ps[63] and enhancing the quantum efficiency to ~44%[63]. Distributed Bragg reflectors[65] and Au nanorods[66] were also used.

Integration with electrically controlled devices allowed electroluminescent generation of SPEs in 1L-WSe_2[43] with $g^2(0)$ ~0.29 (ref. 43). Tuning SPE emission energy is important for multiemitter applications requiring photon indistinguishability. Up to ~21 meV (ref. 67) spectral shift was achieved by applying Stark tuning, ~3.7 meV by strain tuning using a cantilever[68] and ~18 meV by tuning wrinkles with piezoactuators[69].

Spin–orbit coupling in TMDs induces spin splitting in both conduction (tens of meV ref. 26) and valence (hundreds of meV ref. 26) bands, which, in combination with the non-equivalent K points (or valleys) in the first Brillouin zone[26], gives rise to spin–valley locking[26]. This allows for each excitonic valley to be separately addressed and detected by different optical circular polarizations (Fig. 2b). This band structure also contributes to the rich array of different unbound excitonic species in W-based 1Ls, where spectral signatures of semidark excitons are observed along with bright excitons[60] (Fig. 2b).

Given that WSe_2 SPEs can be induced by using patterned substrates, four possibilities have been suggested to explain their origin: (1) strain with the possible brightening of semidark excitons[70]; (2) defects[71]; (3) combination of strain and defects[57,62,72] (Fig. 3b); (4) confinement produced by a different, surrounding dielectric environment[73]. However, none is conclusive yet: correlation between exciton localization and strain has been experimentally reported[74,75], and funnelling of spin-dark excitons into strained regions has been observed[76]. However, the lack of single-photon emission upon application of localized strain was also shown[76].

1L-WS_2 has been less studied than 1L-WSe_2. SPEs in 1L-WS_2 can be deterministically created using the nanopillared substrate approach[58].

https://doi.org/10.1038/s41565-023-01354-x

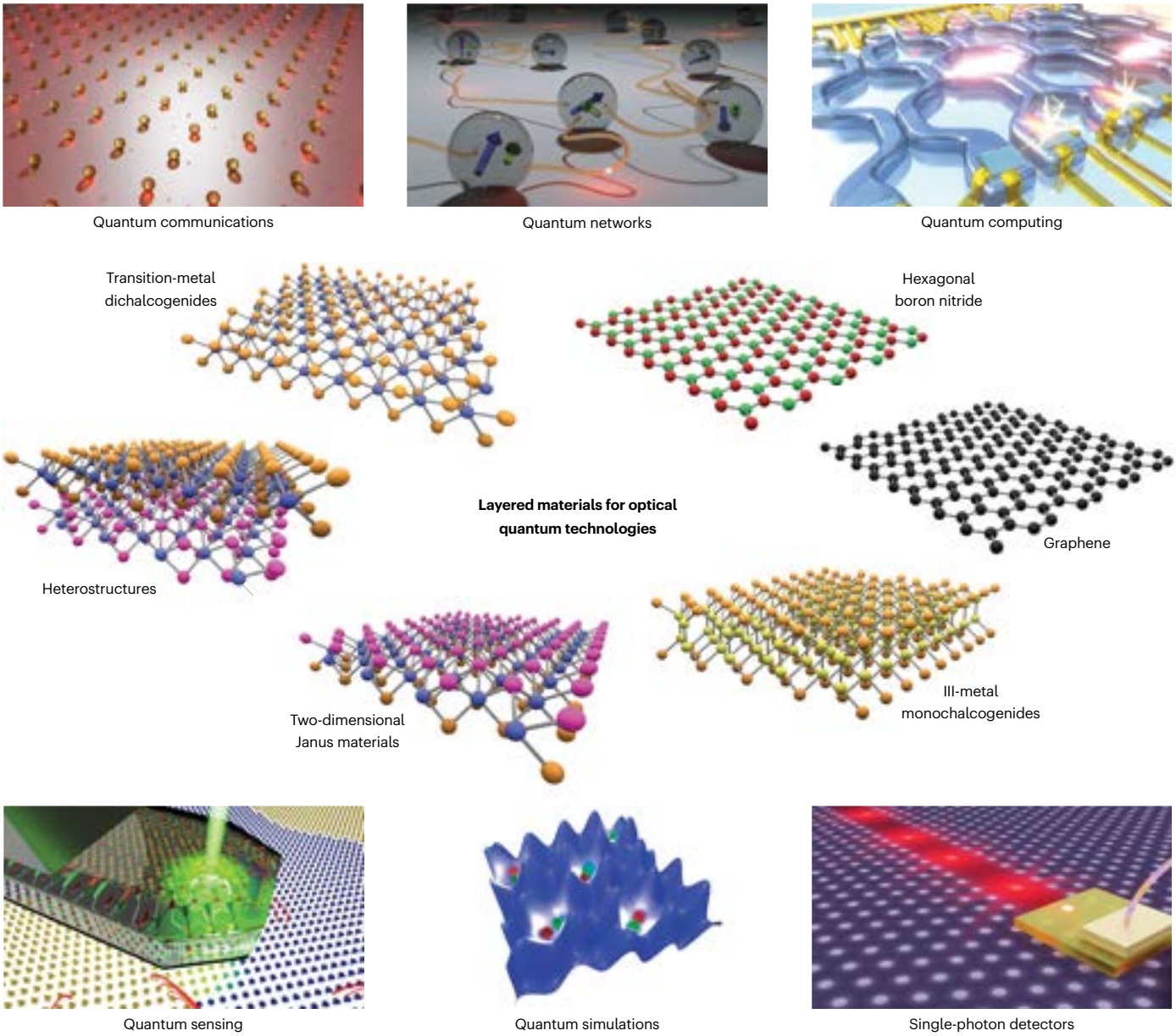

Fig. 1 | Layered quantum materials and optics-based quantum technologies. Inner panels: some LMs that can be used in optics-based QTs. TMDs include WSe_2, WS_2, MoS_2, $MoSe_2$, WTe_2 and $MoTe_2$. TMDs have crystalline phases 2H, 1T, 1T′ and 3R[195]. Here, for all TMDs, including $MoTe_2$, we refer to the semiconducting 2H phase[195]. III-metal monochalcogenides include InSe and GaSe. Janus materials include WSeS and MoSeS. TMDs, III-metal monochalcogenides and hBN host SPEs. Outer panels: QT domains where LQMs can be used: hosts of SPEs for quantum communications, spin–photon interfaces for quantum networks and computing, nanometre-scale sensors, solid-state optical lattice analogues for quantum simulations and single photon detectors. Quantum sensing image adapted with permission from ref. 196, APS.

Electroluminescent single-photon generation was also observed, with $g^2(0) \sim 0.31$ (ref. 43). SPEs in 1L-WS_2 operate at a few K (refs. 43,58), with a fine-structure splitting similar to that of 1L-WSe_2[58], emitting between 1.60 and 1.77 eV (refs. 43,58).

No naturally arising SPEs have been reported thus far for 1L or few-layer 2H $MoTe_2$. However, they can be deterministically generated in 1L-2H $MoTe_2$ using the nanopillar approach[46]. They operate at cryogenic temperatures and have emission wavelengths spanning the entire NIR, up to, and including, the C telecommunication band, from 1.15 to 0.80 eV (1,550 nm) (Fig. 3d). This is important for quantum communications and networks. As the room-temperature thermal energy is below the energy difference between SPE emission and unbound excitons in 1L-$MoTe_2$, SPEs in the telecommunication bands at room temperature could be realizable[46].

1L-$MoSe_2$, bilayer (2L) $MoSe_2$ and few-layer-$MoSe_2$[77,78] also exhibit localized SPEs, typically between 1.57 and 1.63 eV (refs. 77,78). Deterministic positioning was achieved using nanoholes[44]. In contrast to SPEs in 1L-WSe_2, optical lifetimes of SPEs in 1L-$MoSe_2$ are much shorter, ~0.19 ns[44], and the g factor is ~4, similar to unbound bright excitons in 1L-TMDs[26]. In MoS_2, SPEs can be generated by exposure to ultraviolet light[79], and by He-ion irradiation[45] with a spatial accuracy ~9 nm (ref. 80), higher than patterned-substrate approaches, and a yield dependent on the He-ion dose[80]. Some of these defects are unpassivated S vacancies[81] (Fig. 3a), typically between 1.7 and 1.9 eV (refs. 45,80) with a linewidth of hundreds μeV (refs. 45,80). They have the longest lifetime reported thus far amongst all 1L-TMD SPEs, >1 μs (ref. 80), and can be switched on and off by changing the carrier concentration in the host matrix[82]. SPE generation by ion bombardment or

https://doi.org/10.1038/s41565-023-01354-x

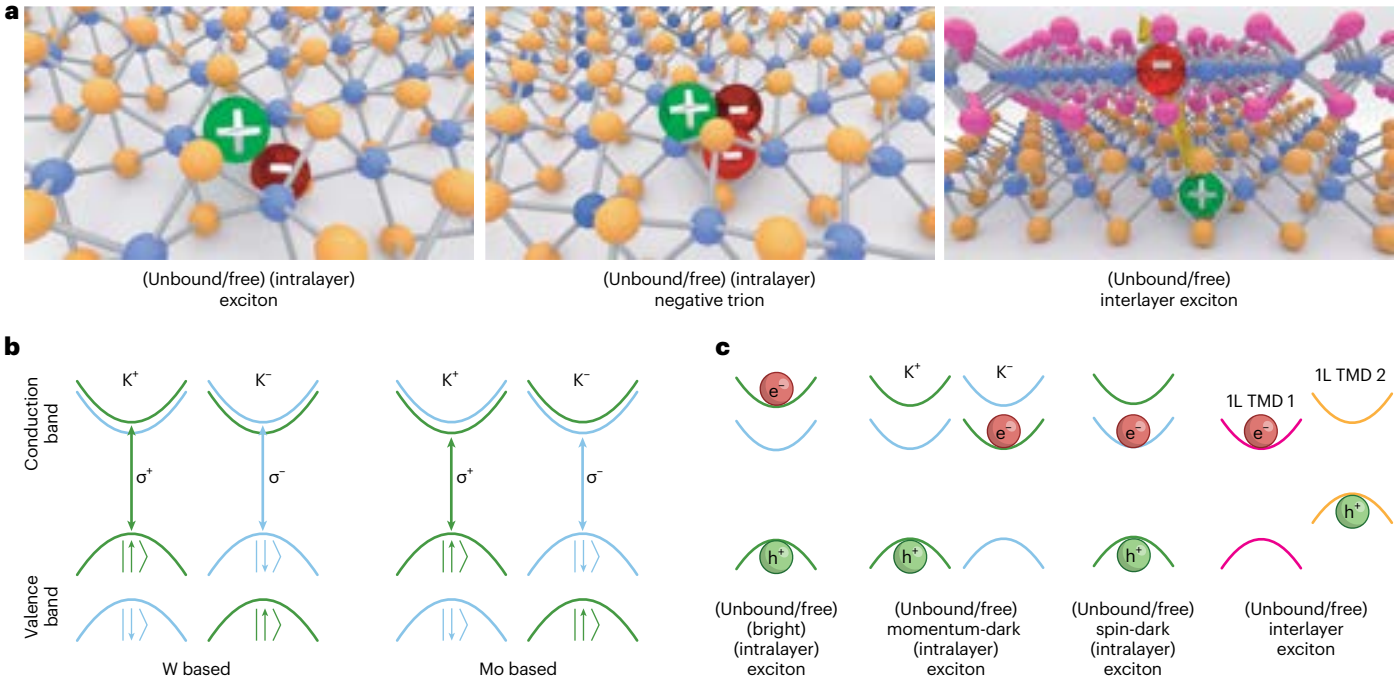

Fig. 2 | Exciton landscape in transition-metal dichalcogenides. **a**, Representation of three types of unbound (or free) excitons in TMDs. A free exciton is an electrostatically bound electron–hole pair. It is different from a confined or localized exciton in that its wavefunction is not constrained to a particular physical TMD location. An intralayer exciton has both electron and hole in the same 1L-TMD. A free negative (positive) trion is an exciton plus an additional electron (hole). A free interlayer exciton has the electron in one 1L-TMD, and the hole in an adjacent 1L-TMD. This charge separation induces a non-zero electric dipole moment (yellow arrow). The words 'free' and 'unbound' are sometimes used to emphasize the nature of the exciton. E.g., 'exciton' and 'free intralayer exciton' are synonyms. **b**, Band structure of W-based and Mo-based 1L-TMDs. K^+ and K^- are the two non-equivalent points, or valleys, in the first Brillouin zone, which can be selectively accessed using right- (σ^+) and left- (σ^-) circularly polarized light, respectively. Assignment of an exciton to either valley is also known as valley degree of freedom, or valley pseudospin. **c**, First three panels: band structure representation of some free excitonic species in a W-based 1L. Only the topmost component of the valence band is depicted. Bright intralayer excitons (or, simply, excitons) are both spin and momentum allowed. A momentum-dark exciton is spin allowed, but momentum forbidden. The opposite applies to a spin-dark exciton. Rightmost panel: band structure representation of an interlayer exciton.

defect implantation has not been reported yet in other TMDs, exemplifying the debate on the nature of SPEs in TMDs: defect-bound excitons, intrinsically detuned excitons, or both.

While one of the LM assets is their reduced dimensionality, being their own interfaces makes them sensitive to local doping, electric fields, dielectric environment, strain and type of substrate[26]. SPEs in LMs are likewise affected by these factors. Their linewidth[38–42] under non-resonant excitation is a few hundred μeV (refs. 38–42), over one order of magnitude broader than their lifetime limit[83] of up to tens of ns (ref. 83). They also suffer from spectral diffusion[38–42,58], and the energy distribution is large (hundreds meV, refs. 38–42,58,62). Efforts to reduce these include using hBN as a substrate[84] and for encapsulation[85], to shield TMDs from the substrate and yield narrower emission lines for unbound excitons[85]; using substrate engineering[86] or plasmonic nanocavities[63], yielding reduced linewidth down to tens μeV; different nanopillar shapes[74] and low-defect LMs (currently 10^9–10^{10} defects cm^{-2}, ref. 48). A combination of strategies, including Stark tuning, improved fabrication and photonic control, is needed to achieve reliable and accurate control of SPE emission properties, especially their emission energy.

Hexagonal boron nitride

SPEs in ML and 1L-hBN can operate at room temperature[47] and can be generated by, e.g., controlled diffusion processes during the chemical-vapour deposition growth of hBN[87], or using irradiation[88].

In contrast to SPEs in WSe_2 and other TMDs, there is a consensus that SPEs in hBN are different optically active point defects[89]. The emission energies spanning NIR[90] to ultraviolet[91], as well as varying response to external magnetic fields[47,92], suggest that defects are of multiple classes. The nature of some of these defects has been studied[90,93,94] (Fig. 3a,e,f): they include carbon-antisite centres in a charged form, $C_BV_N^-$ (ref. 94); C trimers[95,96]; negatively charged B vacancies, V_B^- (ref. 90); and donor–acceptor pairs[97]. Others still need to be assigned[93]. The most studied hBN SPEs to date are V_B^- (ref. 90) and C-related defects[36]. Experiments on V_B^- were done on ensembles[90] only, and it is still a challenge to address single V_B^-, requiring precise control over their position.

In terms of photon indistinguishability, SPEs in hBN suffer from problems similar to those in TMDs: they are prone to being affected by the environment, and the emission properties can be hard to control. Strain is not needed to activate SPEs in hBN[93], but it can be reversibly used to tune emission wavelength and linewidth[98]. Stark shift can change the emission energy over frequencies four times larger than the emission linewidth[99], and some SPEs in hBN can be turned on and off by applying a voltage[100].

SPEs in hBN have also been integrated with metallo-dielectric antennas[101], microcavities[102] and Si_3N_4 photonic crystal cavities[103]. Cavities and waveguides can be also fabricated from hBN itself[104], allowing for monolithic integration.

Some hBN defects, in particular C impurities and V_B^-, can act as spin–photon interfaces: the spins in these SPEs can be optically initialized and read out, and be manipulated by microwaves[36,90,105]. Other unassigned defects also exhibit a response to magnetic fields[106], potentially a spin–photon interface.

https://doi.org/10.1038/s41565-023-01354-x

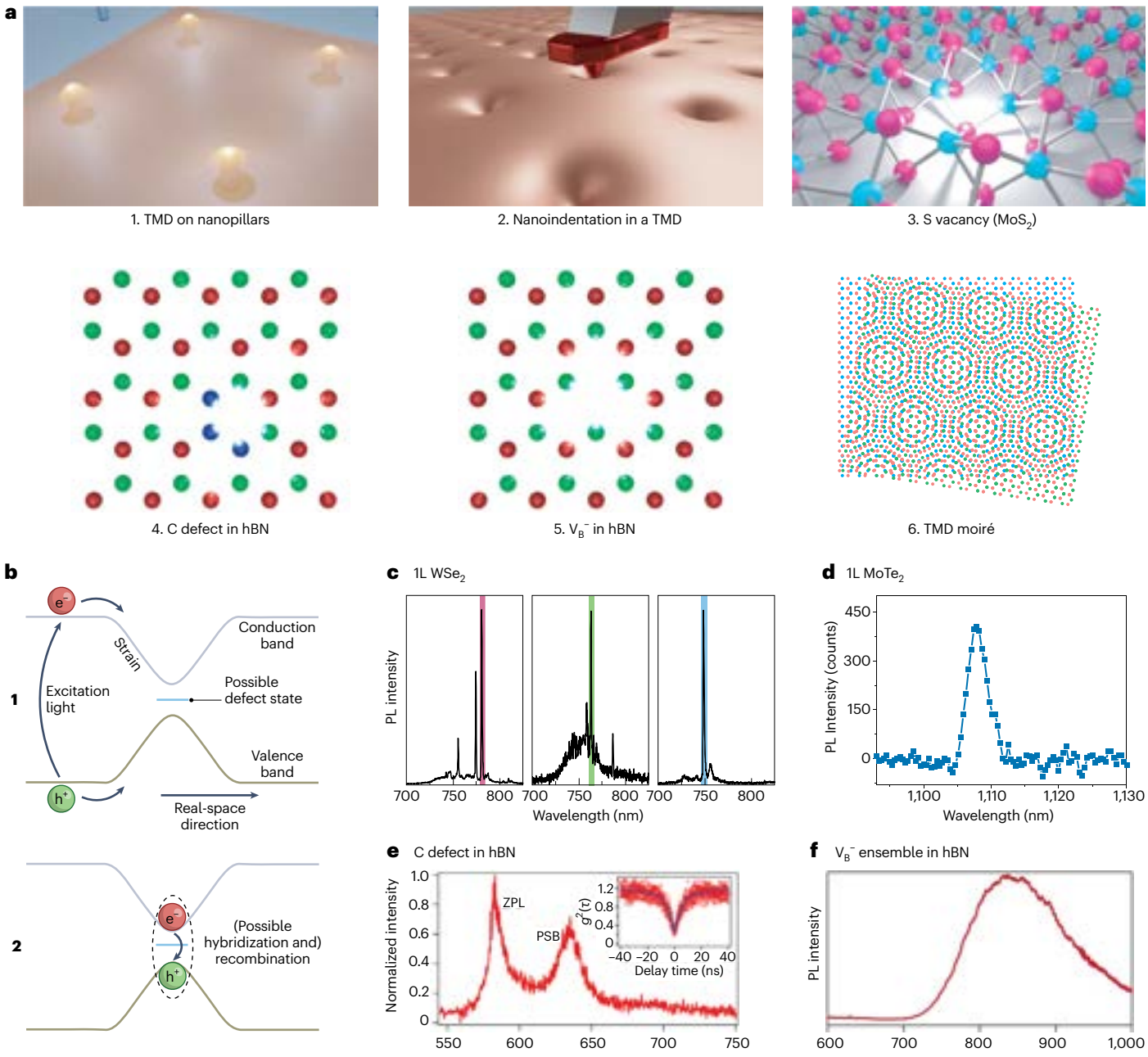

Fig. 3 | Generation and photoluminescence spectra of single-photon emitters in monolayer transition-metal dichalcogenides and in hBN. a, Schematic representation of some methods used to generate SPEs in TMDs and hBN: placing a 1L-TMD on nanopillars; using an atomic-force microscope tip to nanoindent a 1L-TMD on a soft substrate; bombarding 1L-MoS_2 with He ions to generate S vacancies; generating C defects (blue spheres) and B vacancy defects in hBN; generating a moiré pattern. **b**, Possible origin of SPEs in 1L-TMDs. With defects homogeneously distributed across a 1L-WSe_2, or induced by the presence of a nanopillar, spin-dark excitons are funnelled to the bottom of a locally isolated potential well, which may result from the bandgap modulation induced by a nanopillar underneath the 1L. Then, the spin-dark excitons hybridize with the corresponding defect state in that location and recombine, emitting single photons. **c**–**f**, Representative PL spectra of common SPEs in LMs. The spectra from 1L-WSe_2 and 1L-$MoTe_2$ were obtained at cryogenic temperatures and using the nanopillar approach. The spectra from hBN were obtained at room temperature. PSB, phonon sideband. Inset in **e**: photon-photon correlation measurement of C defect in hBN. Panels adapted with permission from: **c**, ref. 58 under a Creative Commons licence CC BY 4.0; **f**, ref. 90, Springer Nature Limited. Panels reproduced with permission from: **d**, ref. 46 under a Creative Commons licence CC BY 4.0; **e**, ref. 94, Springer Nature Limited.

Layered materials heterostructures and moiré lattices

Two stacked 1L-TMDs with different work functions and bandgaps can form an LMH with type-II (or staggered-gap) band alignment. Spatially indirect excitons, known as interlayer excitons[107] (Fig. 2a,c), can then be optically generated.

Interlayer excitons are complementary to intralayer ones, with several advantageous properties. Unbound interlayer exciton wavelengths are closer (up to 1,240 nm, ref. 108) to the telecommunication bands, when compared with intralayer excitons. Their non-zero permanent electrical dipole (up to ~14 e Å in interlayer excitons between non-neighbouring 1Ls[109]) allows for energy tunability over a larger energy range via Stark shift[107], facilitating indistinguishability between photons from different emitters. Their valley lifetime can reach tens µs, with valley selection rules that depend on the stacking

https://doi.org/10.1038/s41565-023-01354-x

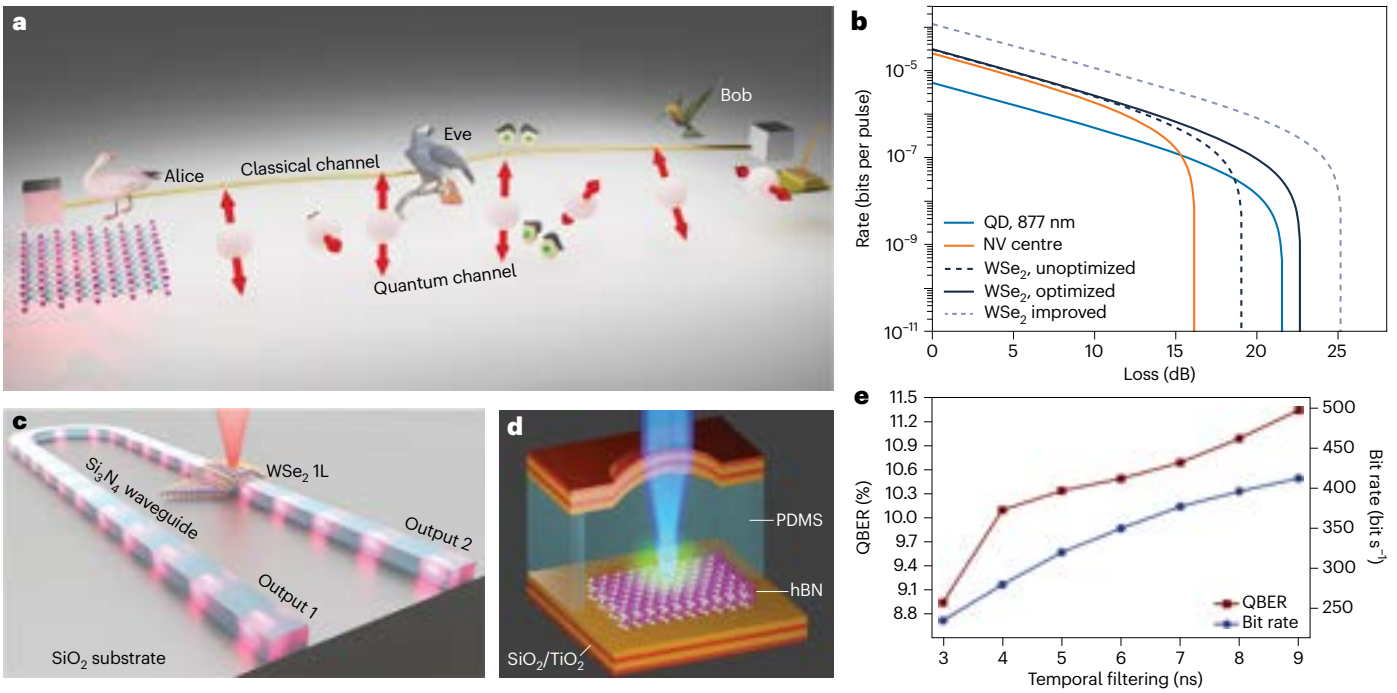

Fig. 4 | Quantum communications with layered quantum materials. **a**, Schematic representation of the QKD protocol BB84, using a 1L-TMD SPE as the single-photon source. Alice sends Bob polarization-encoded (red arrows) quantum information in photons (light red spheres) through a quantum channel. The protocol is completed using a classical channel. If an eavesdropper, Eve, disturbs the communication sufficiently, Alice and Bob will know, and start the protocol again. **b**, Rate-loss diagram of a WSe_2 SPE benchmarked against other platforms for BB84 QKD experiments, revealing its competitiveness in terms of secure bits per pulse, and tolerable losses, if optimization routines are applied. **c**, Schematic integration scheme of TMD SPEs with Si_3N_4 waveguides. The 1L-TMD is deposited on top. SPEs may be generated by the waveguide edges locally straining the LM. **d**, Schematic hBN SPE–microcavity coupled device suitable for QKD applications. **e**, Quantum bit error ratio (QBER) and key rates as a function of detection region duration in a QKD B92 protocol using hBN SPEs. Panel **b** adapted with permission from ref. 122 under a Creative Commons licence CC BY 4.0. Panels reproduced with permission from: **c**, ref. 197 under a Creative Commons licence CC BY 4.0; **d**, ref. 102 under a Creative Commons licence CC BY 4.0; **e**, ref. 130, John Wiley & Sons Inc. Credit: bird icons in **a**, public domain pictures under a Creative Commons licence CC 0.

angle[107]. Interlayer exciton lifetimes are tunable using an external electric field[107], and can be extended to hundreds µs by deviating from high-symmetry stacking angles of 0° and 60°, thanks to the reduced overlap between electron and hole wavefunctions suppressing the recombination rate[48]. The extended lifetimes could allow for the thermalization of all interlayer excitons within a cloud, as well as to the lattice temperature. This opens a promising route towards correlated many-body states of dipolar exciton gases with long-range interactions, a viable platform for solid-state quantum simulations.

Moiré patterns[110–113] (Fig. 3a) are thus far the most common confinement traps for interlayer excitons, exhibiting saturating emission, followed by patterned substrates with pillars[48–51]. Moiré excitons arise when two 1L-TMDs are stacked at a small (<15°) angle with respect to a sixfold symmetric axis[114], with superlattice reconstruction if the LMs have similar lattice constants, and very small stacking angles (<2°). This creates a periodic modulation in the potential energy landscape for interlayer excitons, which can be trapped in the local minima of the perturbation[114]. This could potentially allow for a regular array of indistinguishable, interlayer exciton-based SPEs[115]. The moiré pattern could act as a solid-state analogue of a cold-atom simulator[114], with the periodic trapping potential given by the moiré landscape, rather than a laser trap.

Typically, SPEs arising from moiré patterns in 1L-$MoSe_2$/1L-WSe_2 LMHs are in the NIR, between 1.3 and 1.4 eV (refs. 52,112), or 1.25–1.3 eV for 2L-$MoSe_2$/1L-WSe_2 (ref. 116). The linewidth is hundreds µeV or less[52,112], with a lifetime of >10 ns (refs. 52,112). The number of reports showing moiré SPEs with $g^2(0) < 0.5$ is limited[52], possibly due to the spectral overlap of emission lines, their lower intensity when compared with SPEs in 1L-TMD, an undetermined number of emitters at the same wavelength, or other factors. Moiré trions have been reported[114], laying the foundations for spin–photon interfaces with moiré excitons. Moiré effects were observed in reflectivity and photoluminescence (PL) of unbound excitons in other TMD combinations, for example 1L-WSe_2/1L-WS_2 and 1L-$MoSe_2$/1L-WS_2 (ref. 114).

Other layered materials

Another platform for generating excitons with spatially separated electron–hole wavefunctions are 1L-Janus TMDs[117], in which the crystal plane of transition-metal atoms is sandwiched between two planes, each made of a different chalcogen atom, thus breaking mirror symmetry[117]. This gives rise to Rashba splitting, piezoelectricity, and enhanced second-harmonic generation[118], among others. The different chalcogen atoms have different electronegativities, which generate a built-in electric field that displaces the electron–hole wavefunctions[117]. Advances in Janus synthesis[119,120] have allowed for the integration of Janus 1L-WSeS in hBN-encapsulated charge-controlled devices[55], and the experimental identification of several unbound exciton complexes: neutral free excitons, negatively charged free intervalley/intravalley trions[26] and six particle excitons[121], with optical linewidths similar to those of TMDs[55]. Additionally, SPEs in Janus 1L-WSeS have also been detected[55]. An immediate next step is measuring the out-of-plane electric dipole moment of excitons in 1L -WSeS by applying an out-of-plane electric field in a capacitor-like structure.

The III-metal monochalcogenide group also hosts SPEs. SPEs in ML-GaSe can operate up to room temperature[53], with emission between 1.7 and 2 eV (refs. 31,53). They have been integrated with waveguides

https://doi.org/10.1038/s41565-023-01354-x

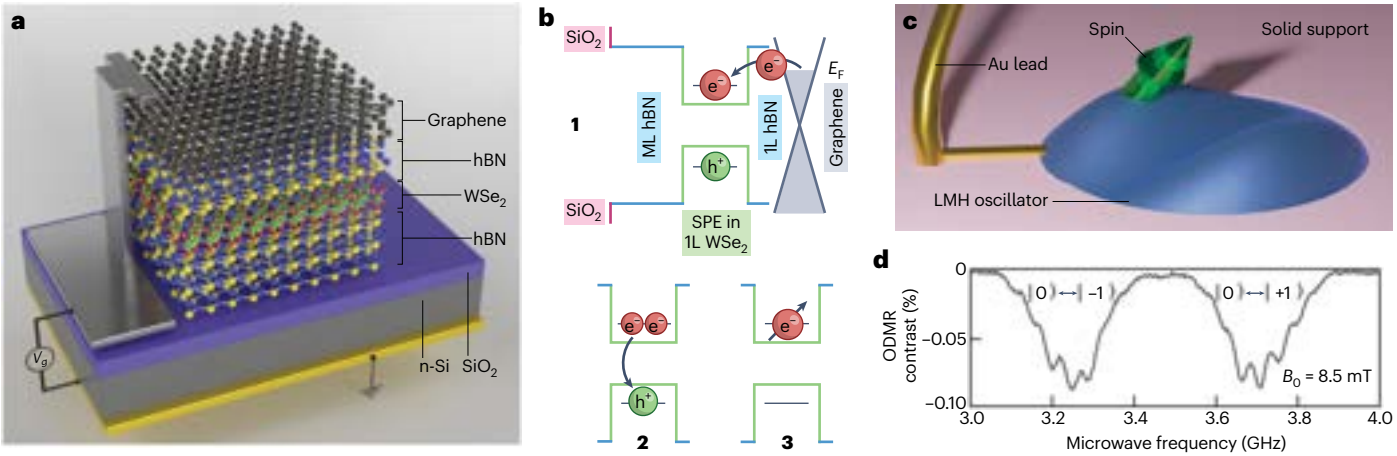

Fig. 5 | Spins in transition-metal dichalcogenides and hBN. a, Schematic of the device used to deterministically charge SPEs. It consists of a FLG charge reservoir, an hBN tunnel barrier, the optically active 1L-WSe_2 containing SPEs, and the hBN barrier underneath. **b**, Schematic of the process to generate optically active spin qubits in 1L- WSe_2. First, a localized potential in a 1L-WSe_2, with our without a trapped exciton, is deterministically charged with an electron tunneling through the 1L-hBN. Second, given the presence of a trion complex, an electron and the hole recombine, emitting a photon. Third, the remaining electron preserves the information in its spin. This structure thus constitutes an optically active spin qubit, where the photon can be used for quantum entanglement and/or optical readout. **c**, LMH (blue) acting as an optomechanical oscillator on a solid support (pink), containing a spin (green) from a reservoir driven by applying a voltage (Au leads). **d**, Room-temperature ODMR contrast from V_B^- centres at ~8.5 mT. Panel **a** adapted with permission from ref. 131, Springer Nature Limited. Panel **d** reproduced with permission from ref. 148 under a Creative Commons licence CC BY NC 4.0.

with coupling efficiency >3.5% (ref. 31). Saturating emission was observed in ML-InSe between 1.3 and 1.36 eV (ref. 54).

Layered materials for optical quantum technologies

Quantum communications

Given their cost-effectiveness, scalability and ease of integration with photonic structures for improved count rates and signal-to-noise-ratio, LMs are ideal as quantum key distribution (QKD) platforms (Fig. 4a). Deterministically created SPEs in 1L-WSe_2 emitting in the NIR have been used to emulate the BB84 protocol with a photon flux rate of tens kHz and a quantum bit error ratio ~0.7% with $g^2(0) < 0.1$ (ref. 122) (Fig. 4b). To further enhance the QKD application capabilities of SPEs in TMDs, efforts have been devoted towards controlling polarization[123], emission wavelength[67–69] and position[58,62,63], for improved cavity coupling. Optimization of TMD SPE coupling to plasmonic[32], $LiNbO_3$[124] and Si_3N_4[125] waveguides depends on the same parameters. So far, most coupling strategies have relied on placing a 1L-TMD on top or on the side of a waveguide, and examining whether SPEs are generated in the vicinity of the photonic structure[124,125] (Fig. 4c). Further progress in deterministic positioning and optical properties of SPEs in TMDs is required to improve coupling efficiency into waveguides beyond the current <10% (refs. 124,125). Cavity-coupled TMD quantum light-emitting diodes would allow for all-electrical generation of single photons with deterministic optical properties and enhanced emission rate.

The suitability of LMs for space QKD has been studied in terms of resistance to typical space high-energy irradiation[126,127]. While all studied LMs, except WS_2, resist irradiation[127], hBN additionally offers single-photon operation at room temperature and up to 800 K (ref. 126). The small footprint of LMs can be leveraged to package hBN SPEs coupled to tunable microcavities as self-contained single-photon sources, in addition to a confocal microscope, onto satellites with volume of <1 litre, where they could be used for both QKD and to test fundamental postulates of physics[128].

Efforts were made to enhance the collection efficiency of hBN SPEs and their coupling to photonic structures (Fig. 4d), with challenges similar to TMDs. hBN SPEs emitting at MHz rates with $g^2(0) < 0.1$ were realized by integrating hBN with a solid immersion lens[129]. Under these conditions, a secured key rate >10^5 is realistic within city boundaries of ~8 km (ref. 129). hBN SPEs have been integrated in a proof-of-concept QKD B92 protocol at room temperature with a quantum bit error ratio ~10% and transmission key rate ~500 bits s^{-1} (ref. 130) (Fig. 4e).

Spins and photons for quantum networks and computation

Additional charges can be introduced in 1L-WSe_2 SPEs[131], endowing them with a spin. A device structure consisting of few-layer graphene (FLG), 1L-hBN, 1L-WSe_2 and ML- hBN (Fig. 5a) allows for voltage-controlled tunnelling of electrons (or holes) from the FLG reservoir through a 1L-hBN barrier into the trap potential in 1L-WSe_2, enabling the generation of confined trions. The extra electron that remains after an electron–hole recombination process provides the long-lived two-level spin system, similar to other optically active spin qubits[4] (Fig. 5b). Localized trions can also be obtained in a ML-hBN-encapsulated 1L-WSe_2/2L-CrI_3 (ref. 132), where the 2L-CrI_3 transfers the required charge to the 1L-WSe_2.

Indistinguishable photons are needed for entanglement between separate emitters[4]: resonant fluorescence of stable and Stark-tunable emitters and Hong–Ou–Mandel experiments to measure photon indistinguishability are still to be performed. Given that SPEs in TMDs have shown biexciton (two electrons and two holes bound together) emission[133], they could be a source of entangled photons by biexciton cascade[134].

The valley degree of freedom in TMDs could be used as a two-level system for quantum information processing. However, several challenges must be overcome. Although manipulation of valley pseudospin in unbound excitons has been demonstrated using both optical means and static magnetic fields[26], valley depolarization of unbound excitons and trions in ML-TMDs happens over timescales of a few ps (ref. 26). The valley coherence time ~350 fs for free excitons[26] is currently too short for valley qubits, and should be enhanced for meaningful quantum-information processing based on the valley degree of freedom. Alternatives include using optically active resident charge carriers, with valley relaxation time >100 ns for electrons[135] and ~2 µs for holes[135]. In regard to TMD SPEs, it is still unclear to what extent the valley pseudospin picture can be transferred to them. The Landé g factor in confined excitons and negatively charged trions ($g \sim 7–9$)[131] may indicate that both spin and valley play a prominent role in the SPE

https://doi.org/10.1038/s41565-023-01354-x

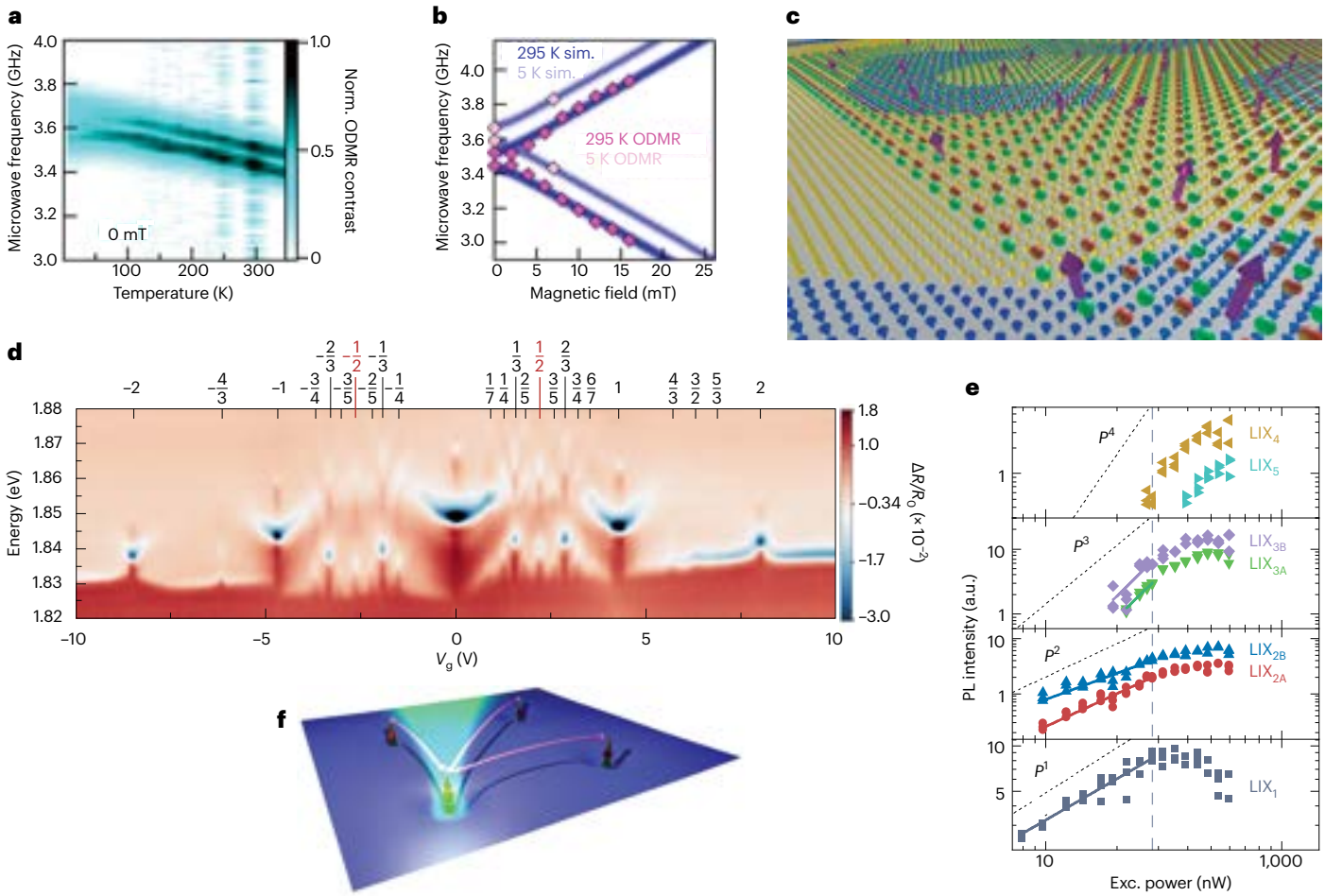

Fig. 6 | Layered quantum materials for quantum sensing and simulations. **a**, ODMR spectra of V_B^- hBN defects as a function of temperature. **b**, OMDR spectra of V_B^- hBN defects as a function of an external magnetic field. **c**, 1L-hBN (green and red spheres) containing an ensemble of spins (purple arrows) on a magnetic substrate. The spin ensemble can be used as sensors to probe the magnetic domains (yellow and blue cones) of the underlying substrate. **d**, Spectrally resolved reflectivity contrast of a moiré 1L-WSe_2/1L-WS_2 at 6 K for different applied voltages (corresponding to different electron fillings). It shows correlated insulating states at fractional fillings of the moiré lattice. **e**, Power-dependent PL intensity of localized interlayer excitons in 1L-$MoSe_2$/1L-WSe_2 at 10 K, up to P^4 (with P the laser power), showing that localized sites can host multi-interlayer exciton complexes. a.u., arbitrary units. **f**, Long-range dipolar interaction (pink arrows) arising between pairs of interlayer excitons (green and red spheres) with non-zero electric dipole moment and separated beyond the laser diffraction limit (green). Panels adapted with permission from: **a**, ref. 149, Springer Nature Limited; **e**, ref. 49, Springer Nature Limited. Panels reproduced with permission from: **b**, ref. 149, Springer Nature Limited; **d**, ref. 198, Springer Nature Limited.

structure and optical selection rules. For positively charged trions, the Coulomb terms that cause valley mixing are quenched[136]. In 1L-MoS_2, the valley picture can be transferred to SPEs generated by defects[137]. A final proof of the presence and extent of valley pseudospin in TMD SPEs is still lacking.

Transmitting quantum information between non-optically active qubits over long distances requires coherent microwave to optical photon conversion, and vice versa. Optomechanical systems are being investigated[138] for this. Suspended membranes of 1L-WSe_2[139] and 1L-$MoSe_2$[140] were fabricated with quality factors in the 10^5 range[139,140] (compared with 10^9 for Si_3N_4 membranes[141] and crystalline Si[142]) and resonance frequencies in the tens MHz (refs. 139,140). SPEs in 1L-WSe_2 were acoustically controlled via integration with a surface acoustic wave resonator[143]. Besides microwave–optical photon conversion, optomechanical membranes with proximal spins would allow for quantum entanglement of non-classical states of motion with quantum two-level systems for quantum sensing[144], and for testing fundamental quantum mechanics[145] and gravity[146]. While the spin does not necessarily need to be embedded in the membrane for spin–oscillator coupling, this would allow for stronger interactions and no need for mediation via, e.g., magnetic-field gradients. Therefore, TMDs or hBN acting as membranes, and with embedded SPEs with spin, are an ideal platform for this (Fig. 5c). The first challenge would be to tune the resonance frequency of the membrane closer to that of the spin transition, while improving the quality factor. At the same time, for 1L- TMDs, the device would have to allow for the presence of charged SPEs, possibly in an LMH similar to that used to charge SPEs in 1L-WSe_2[131]. Finally, the response of SPEs with strain in such a device would have to be thoroughly investigated.

In contrast to TMDs, SPEs in hBN operate at room temperature and have phonon sidebands energetically separated (by as much as a few hundred meV (ref. 147)) from the coherent ZPL. Some hBN defects have shown ODMR (Fig. 5d) and spin Rabi oscillations[148]. Room-temperature ODMR on ensembles of V_B^- shows a triplet ground state with a zero-field splitting ~3.6 GHz (ref. 90). In contrast to V_B^- defects, where the quantum efficiency must still be increased to reach the single-spin regime, ODMR signals have been observed on single C impurities in hBN[36]. The spin T_2 measured to date in any hBN defect is of the order of hundreds ns, or a few µs (ref. 105), still far from the tens ms and even s achieved in diamond[4]. Extending the coherence time will require careful consideration of the decoherence mechanisms in hBN.

Quantum sensing

hBN defects with spin can be used as sensors. They are sensitive to temperature (Fig. 6a), magnetic fields (Fig. 6b) and pressure, and can thus be used as detectors for these quantities[149]. Much like nitrogen–vacancy (NV^-) centres in diamond[4], a single hBN defect with spin could be used for non-invasive static magnetic-field detection via scanning ODMR (whose contrast can be plasmonically enhanced[150]) by attaching hBN to a cantilever with electrical readout (Fig. 1). Due to the 1L nature, defects in 1L-hBN can be in very close proximity to a magnetic substrate, enhancing spatial resolution[151], as well as detecting stray fields from a weaker magnetization[152]. Homogeneously distributed ensembles of V_B^- defects can be addressed at once in an hBN flake, with size of tens µm on a magnetic substrate, to extract a space-resolved ODMR signal[153] (Fig. 6c). This may enable the observation of time-dependent magnetic processes, but with reduced resolution when compared with using a single spin.

TMDs can also be used as magnetic probes by placing them in close proximity to magnetic materials, and exploiting their polarization-dependent optical selection rules[35]. In this case, the resolution is given by the set-up optical diffraction limit.

Quantum simulations and dipolar particles

TMD moiré superlattices as hosts of regularly spaced wells for excitons[115] face two challenges. (1) Moiré superlattices, as well as reconstructed structures, generally allow for subdiffraction spacing between SPEs, as the characteristic length scale is of the order of tens nm or less[114], depending on the lattice parameters of the constituent layers and their stacking angle[114]. (2) Real-space images have shown that, in practice, perfect crystallinity of moiré superlattices is not retained beyond the µm range[114], meaning that there is considerable variation within an extended TMD moiré superlattice[114]. Ideally, moiré-based studies, especially those probing large areas (>1 μm^2), should also provide real-space images.

Despite reports showing resolvable saturating emission[112] and $g^2(0) < 0.5$ (ref. 52), using moiré superlattices as a source of indistinguishable single photons is still a challenge. Investigations should also focus on the origin of the emission from moiré-confined excitons. Reference 154 reported localized emission from interlayer excitons in 1L-$MoSe_2$/1L-WSe_2 with properties similar to those of moiré-trapped excitons, but in the absence of a moiré potential.

Although LM moiré lattices do not have the degree of control that atoms offer, and reproducibility can be challenging, the number of different LMs available[22,23,28], in conjunction with their almost endless possible combinations and stacking angles, promise new avenues for the exploration of quantum simulations as solid-state optical lattice analogues[155]. TMD moiré superlattices have already shown correlation-driven phases[114] (Fig. 6d) and non-trivial band topology[114]. Although the techniques for experimentation with moiré superlattices are usually transport-based, optical approaches can also be used, including for the induction of ferromagnetism in 1L-WS_2/1L-WSe_2[156]. The individual optical addressing and control of sites in moiré superlattices in the Hubbard model[114] will require near-field optical microscopy. Future models to be constructed with TMDs/hBN and beyond include Kagome lattices[157] or Hubbard–Kanamori models[158].

The nanopillar approach with TMD-based LMHs that exhibit type-II band alignment yields arrays of confined interlayer excitons[48–51] that can exhibit very high single-photon purity (down to $g^2(0) \sim 0.01$)[50] and operate up to 77 K (ref. 50). With sites separated beyond typical diffraction limits of ~1 µm, and wavelengths closer to the telecom bands, this approach to generate SPEs in TMD LMHs is promising for quantum communications. However, the materials need to be carefully engineered, and the confinement generation mechanisms well understood. Hybridized band structure and defect-state arguments have been used to explain nanopillar-induced interlayer SPEs[50]. Confined interlayer excitons generated using nanopillars can show discrete intrasite dipolar interactions[49] (Fig. 6e), potentially serving as a source of entangled photons. They can have optical lifetimes >1 µs (ref. 48), higher than the dipolar interaction rate between SPEs at distances beyond typical diffraction limits of ~1 µm (ref. 48) (Fig. 6f). Much like Rydberg atoms in optical lattices[2], they could thus be used in a trap array to simulate quantum spin Ising-type systems and perform Ising-based quantum annealing for quantum computation. TMD-LMHs would then be an on-chip quantum simulator not requiring complex trapping schemes. However, the non-zero electric dipolar moment of interlayer excitons makes them prone to being more affected by external electric noise when compared with intralayer excitons. Thus, dipolar interactions between distant (>1 µm), single, confined interlayer excitons still need to be shown.

Signatures of Bose–Einstein condensation were observed in TMD-LMHs >100 K (ref. 159), leading to the study of Bose–Einstein condensation at high temperatures and applications based on condensates. Bose–Einstein condensates composed by dipolar particles, interacting over long ranges (beyond nearest neighbours), would enable the generation and study of novel coherent phases in the solid state[160].

1L-Janus materials[161] are an alternative to type-II LMHs to generate dipolar excitons. Because they are 1L, they may avoid the presence of random interface irregularities that pose challenges in LMHs for the observation and interpretation of long-range coherent phenomena in clouds of dipolar excitons. The electric dipolar moment of Janus excitons was calculated to be smaller than that of interlayer excitons in TMD-LMHs, ~0.038 e Å in 1L-MoSeS[162] in comparison with the measured ~6.03 e Å in 1L-$MoSe_2$/1L-WSe_2[163]. Because of this, the observation of any dipolar-related phenomenon, such as emission blueshift[49], will probably require the trapping of excitons by, for example, electric fields. Additionally, the dipolar moment of Janus excitons in moiré heterobilayers has been predicted to enable high-temperature Bose-Einstein condensation[164].

The patterning of nanoislands[165], if sufficiently small, could generate an SPE array suitable for quantum communications. The nanoislands could be of a Janus material embedded within 1L-TMDs[166], leading to SPEs that can interact over distances beyond their nearest neighbours. A periodically patterned dielectric in proximity to a 1L-WSe_2 is another strategy that could produce an array of SPEs for interlayer excitons based on moiré bands[73].

Single-photon detectors

QTs based on optically active qubits, including QKD protocols, LOQC, or quantum simulations, demand not only high-purity SPEs, but also suitable readout devices: single photon detectors (SPDs)[1,167,168].

On-chip integration of SPDs for photon-based quantum information processing may lead to a reduction of photon loss. This is critical, for example, for efficient LOQC, which imposes stringent conditions on overall permissible photon loss[169]. Superconducting-nanowire SPDs can help overcome this[170], but in a device consisting of LMs it may be desirable to integrate a LM-based detector.

A promising approach for using LMs as SPDs is by exploiting their superconducting properties, following the same principle as other superconductor-based SPDs. E.g., two twisted single layer graphene (SLG) stacked at a 'magic angle'[171] give rise to a superconducting phase. In this regime, magic-angle graphene may overcome the wavelength limitations of superconducting transition-edge sensors and superconducting-nanowire SPDs by virtue of its thinness and high electron density, potentially extending the detection bands to the far IR and THz[37]. Given the low absorption of SLG (2.3% for photon energies >0.5 eV for suspended SLG, ref. 22), such a device will have to be coupled with other photonic structures, such as photonic cavities, to reach efficiencies comparable to current alternatives.

Non-graphene LMs may increase the bottom-line absorption of SLG, and overcome the need of relying on carefully aligned moiré superlattices to exploit graphene superconductivity, while still retaining

https://doi.org/10.1038/s41565-023-01354-x

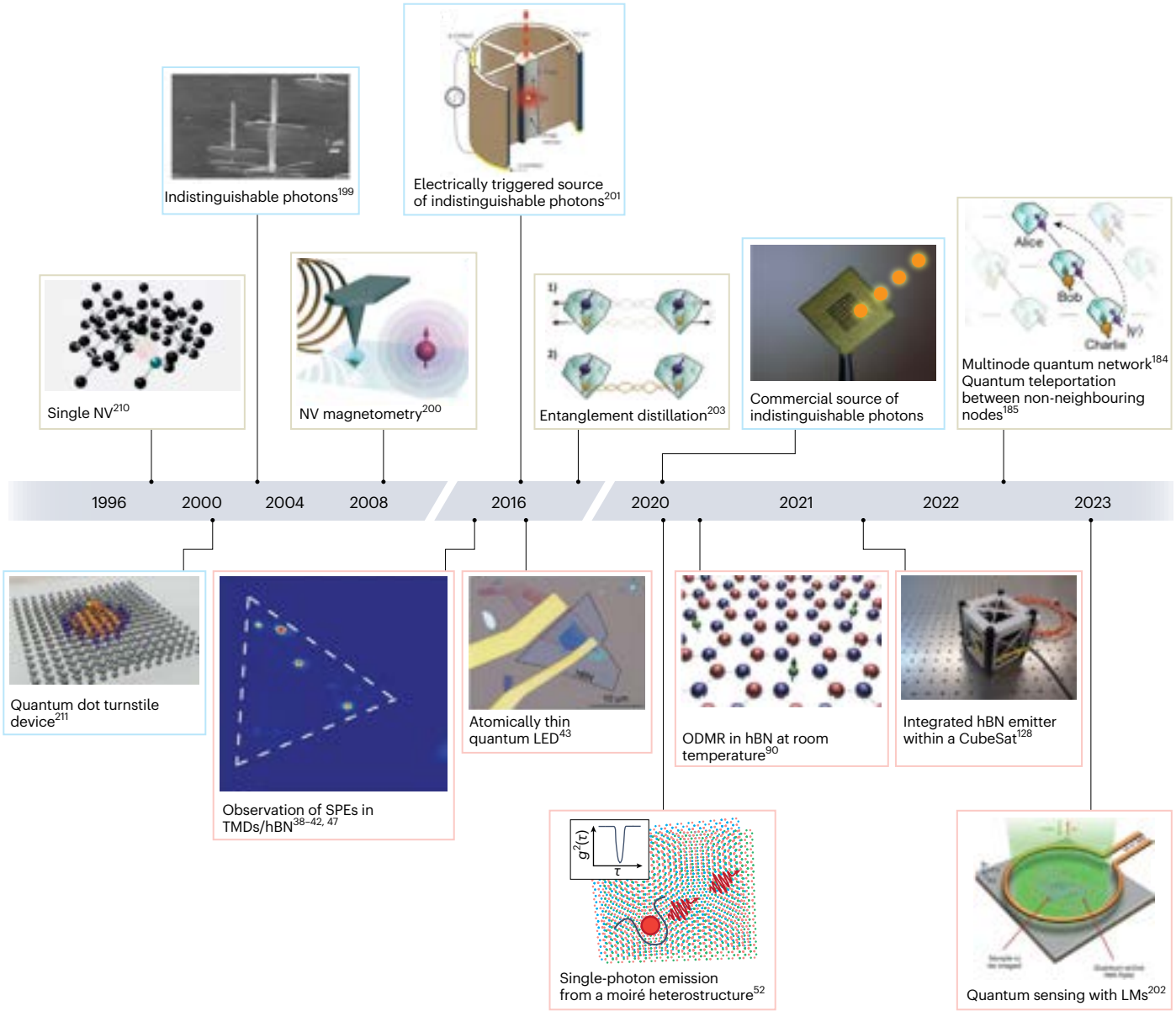

Fig. 7 | Some milestones in the evolution of layered quantum materials-based quantum technologies, compared with mature platforms. Blue squares are related to research done on semiconductor QDs, green squares to NV^- centres in diamond, and pink squares to LQMs. Given the rapid development of hBN and TMD-based SPEs, LQM-based QTs could be viable within the next 10 years. Panels reproduced with permission from: indistinguishable photons, ref. 199, Springer Nature Limited; NV magnetometry, ref. 200, Springer Nature Limited; electrically triggered source of indistinguishable photons, ref. 201, Springer Nature Limited; quantum teleportation between non-neighbouring nodes, ref. 185, Springer Nature Limited; atomically thin quantum LED, ref. 43, Springer Nature Limited; ODMR in hBN at room temperature, ref. 90, Springer Nature Limited; integrated hBN emitter within a CubeSat, ref. 128 under a Creative Commons licence CC BY 4.0; quantum sensing with LMs, ref. 202, Springer Nature Limited. Panels adapted with permission from: entanglement distillation, ref. 203, AAAS; observation of SPEs inTMDs/hBN, ref. 42, Springer Nature Limited.

reduced film thickness. 1L- and 2L-$NbSe_2$ show superconducting transitions around 2 and 5 K (ref. 172), respectively, and $NbSe_2$-based photodetectors have been reported[173]. Sensitivity down to single-photon level remains elusive, partially due to the challenge of avoiding oxidation of the superconducting layer. While other superconducting LMs have lower electron densities when compared with magic-angle graphene[37], some offer operation temperatures >77 K, such as $Bi_2Sr_2CaCu_2O_{8+\delta}$ in the form of a superconducting-nanowire SPD, for which responsivity and operation speeds comparable to state-of-the-art InGaAs photodiodes, and better than superconducting transition-edge sensors, were shown[174].

Another route for LM-based SPDs is integrating non-graphene LMs as the non-superconducting element in Josephson junctions, then using them as bolometers and photodetectors. SLG-based Josephson junction bolometers embedded in microwave resonators promise much faster operation at higher energy resolution than currently possible, ~10^5 times faster than superconducting-nanowire SPDs at 32 GHz resolution[175], while SLG- and FLG-based lateral Josephson junctions have shown single-photon detection at 1,550 nm in the mK regime, compatible with the working temperature of quantum computers based on superconducting qubits[176].

Outlook

The 2022 Nobel Prize in Physics for quantum information represents a strong driving force for the development of LMs for QT applications,

after the 2010 Nobel Prize for the groundbreaking experiments on SLG, the prototypical LM. We are at the dawn of the era of layered quantum materials (LQMs). The growing library of LMs can play a key role in the future of QTs, but a lot remains to be done. LQMs have potential for quantum algorithms and quantum information using photons. The accessibility to state-of-the-art qubits (whether in hBN or TMDs) will be pivotal to achieve measurable progress. The pace of realizing quantum components in LQMs is outperforming that of traditional bulk systems (Fig. 7). It took less than three years to go from optical[38–42] to electrical[43] excitation of quantum emitters in TMDs, and less than two years to achieve coherent control of an electron spin in hBN[148], after localized spins were identified[90]. These achievements took decades of dedicated research for solid-state quantum systems, Fig. 7.

A better understanding of the underlying nature of SPEs in TMDs will contribute to the reduction in their linewidth and energy distributions, their precise positioning in cavities for optimized Purcell enhancement, coupling to other photonic structures and elucidation of their internal energy structure. More effort is needed to relate measurements of strain via Raman spectrometry with PL measurements at room and low temperature, combined with localized measurements via scanning near-field optical microscopy[177], to elucidate the role played by strain, if any, in the formation of SPEs in TMDs. At the same time, advances in bulk and 1L-TMD synthesis as well as 1L-TMD transfer techniques, together with real-space imaging at the atomic scale, will allow for the observation of possible correlations between the presence of a point or a one-dimensional defect and single-photon emission at specific locations.

Systematic and reliable generation of charged SPEs in TMD is still missing. Once this is accomplished, the next steps, following the historical development of other solid-state SPEs, such as QDs or NV^- centres[4], will be to study the spin energy levels and selection rules, characterize the spin properties and achieve coherent control of the electron spin. Similar studies will be conducted for the hole spin. Electronic coherence times can be potentially enhanced, due to the hyperfine coupling with non-zero nuclear-spin isotope baths being ten times weaker in LMs when compared with semiconductor QDs[178]. Additionally, many of the naturally abundant isotopes that make up TMDs have nuclear spin zero[179], advantageous for extending coherence times. On the other hand, nuclei with a non-zero spin could serve as proximal memory qubits, as done in other solid-state systems[4], thus having the TMD serve as a quantum processor.

The steps to develop SPEs in hBN as spin–photon interfaces for quantum networks and computation are similar to those followed for defects in diamond[4]. Electron paramagnetic resonance measurements show that the hBN spins couple to the nuclear spins of N, C and B[90,180–182], with coherent control of ^{14}N nuclei having been shown[183], which could then be used as ancillary qubits to generate entanglement between nodes[184–186], or cluster states[187] for measurement-based quantum computation[188]. Coupled with advances in meta-optics, hBN could lead to quantum meta-optical systems capable of light generation and manipulation on a single chip. The ability to coherently initialize and read out the electron spin states from some of the hBN defects may be vital to quantum microscopy with nanoscale resolution, surpassing the state of the art[189].

For heterostructures, dipolar excitons in moiré superlattices were proposed as local sensors of correlated electron phases[190], and excitonic insulators were realized[191]. Other platforms that could unveil other low-dimensional many-body phenomena[192] include one-dimensional moiré lattices[192] and strain-induced one-dimensional excitonic channels[193]. This will be aided by advances in material quality and moiré superlattice homogeneity.

The vast library of LMs[23] contains all ingredients to achieve a fully LM-based integrated quantum-photonic device, including optically active spin qubits and SPDs. Selective patterning and lateral heterostructure growth[194] can lead to the design of bandgap-engineered one- and zero-dimensional traps for exciton confinement and routing, and the engineering of emitted light properties. To push the field further, and translate the scientific achievements into technology, the reproducibility of device-to-device engineering and sample-to-sample synthesis must be ensured. The long-term stability of the generated SPEs and moiré heterostructures should be reported, by presenting the response of the quantum devices after thermal cycling, or by studying the bleaching of defect-based SPEs.

Only with a concerted effort can the key challenges of LMs for QTs be overcome: photon indistinguishability, coherent single-spin manipulation, controlled spin–photon interfaces and bright quantum emission in the telecommunication range. The interest in LQM SPEs will keep growing, as coherent control and photonic integration develops for quantum communications and networks, while TMDs may be used for quantum simulators based on strongly correlated and interacting dipolar exciton gases.

References

1. Acín, A. et al. The quantum technologies roadmap: a European community view. *New J. Phys.* **20**, 080201 (2018).
2. Browaeys, A. & Lahaye, T. Many-body physics with individually controlled Rydberg atoms. *Nat. Phys.* **16**, 132–142 (2020).
3. Zhong, H.-S. et al. Quantum computational advantage using photons. *Science* **370**, 1460–1463 (2020).
4. Atatüre, M., Englund, D., Vamivakas, N., Lee, S.-Y. & Wrachtrup, J. Material platforms for spin-based photonic quantum technologies. *Nat. Rev. Mater.* **3**, 38–51 (2018).
5. Gangloff, D. A. et al. Quantum interface of an electron and a nuclear ensemble. *Science* **364**, 62–66 (2019).
6. Gangloff, D. A. et al. Witnessing quantum correlations in a nuclear ensemble via an electron spin qubit. *Nat. Phys.* **17**, 1247–1253 (2021).
7. Zaporski, L. et al. Ideal refocusing of an optically active spin qubit under strong hyperfine interactions. *Nat. Nanotechnol.* **18**, 257–263 (2023).
8. Bar-Gill, N., Pham, L. M., Jarmola, A., Budker, D. & Walsworth, R. L. Solid-state electronic spin coherence time approaching one second. *Nat. Commun.* **4**, 1743 (2013).
9. Bhaskar, M. K. et al. Quantum nonlinear optics with a germanium-vacancy color center in a nanoscale diamond waveguide. *Phys. Rev. Lett.* **118**, 223603 (2017).
10. Trusheim, M. E. et al. Transform-limited photons from a coherent tin-vacancy spin in diamond. *Phys. Rev. Lett.* **124**, 023602 (2020).
11. Higginbottom, D. B. et al. Optical observation of single spins in silicon. *Nature* **607**, 266–270 (2022).
12. Bergeron, L. et al. Silicon-integrated telecommunications photon–spin interface. *PRX Quantum* **1**, 020301 (2020).
13. Chartrand, C. et al. Highly enriched ^{28}Si reveals remarkable optical linewidths and fine structure for well-known damage centers. *Phys. Rev. B* **98**, 195201 (2018).
14. Babin, C. et al. Fabrication and nanophotonic waveguide integration of silicon carbide colour centres with preserved spin-optical coherence. *Nat. Mater.* **21**, 67–73 (2022).
15. Christle, D. J. et al. Isolated spin qubits in SiC with a high-fidelity infrared spin-to-photon interface. *Phys. Rev. X* **7**, 021046 (2017).
16. Bourassa, A. et al. Entanglement and control of single nuclear spins in isotopically engineered silicon carbide. *Nat. Mater.* **19**, 1319–1325 (2020).
17. Kindem, J. M. et al. Control and single-shot readout of an ion embedded in a nanophotonic cavity. *Nature* **580**, 201–204 (2020).
18. Raha, M. et al. Optical quantum nondemolition measurement of a single rare earth ion qubit. *Nat. Commun.* **11**, 1605 (2020).
19. Kornher, T. et al. Sensing individual nuclear spins with a single rare-earth electron spin. *Phys. Rev. Lett.* **124**, 170402 (2020).

20. Högele, A., Galland, C., Winger, M. & Imamoglu, A. Photon antibunching in the photoluminescence spectra of a single carbon nanotube. *Phys. Rev. Lett.* **100**, 217401 (2008).
21. Ishii, A. et al. Enhanced single-photon emission from carbon-nanotube dopant states coupled to silicon microcavities. *Nano Lett.* **18**, 3873–3878 (2018).
22. Ferrari, A. C. et al. Science and technology roadmap for graphene, related two-dimensional crystals, and hybrid systems. *Nanoscale* **7**, 4598–4810 (2015).
23. Mounet, N. et al. Two-dimensional materials from high-throughput computational exfoliation of experimentally known compounds. *Nat. Nanotechnol.* **13**, 246–252 (2018).
24. Gjerding, M. N. et al. Recent progress of the Computational 2D Materials Database (C2DB). *2D Mater.* **8**, 044002 (2021).
25. Iyengar, S. A., Puthirath, A. B. & Swaminathan, V. Realizing quantum technologies in nanomaterials and nanoscience. *Adv. Mater.* **2022**, 2107839 (2022).
26. Wang, G. et al. Colloquium: Excitons in atomically thin transition metal dichalcogenides. *Rev. Mod. Phys.* **90**, 021001 (2018).
27. Cassabois, G., Valvin, P. & Gil, B. Hexagonal boron nitride is an indirect bandgap semiconductor. *Nat. Photon.* **10**, 262–266 (2016).
28. Backes, C. et al. Production and processing of graphene and related materials. *2D Mater.* **7**, 022001 (2020).
29. Aharonovich, I., Englund, D. & Toth, M. Solid-state single-photon emitters. *Nat. Photon.* **10**, 631–641 (2016).
30. Brotons-Gisbert, M., Martínez-Pastor, J. P., Ballesteros, G. C., Gerardot, B. D. & Sánchez-Royo, J. F. Engineering light emission of two-dimensional materials in both the weak and strong coupling regimes. *Nanophotonics* **7**, 253–267 (2018).
31. Tonndorf, P. et al. On-chip waveguide coupling of a layered semiconductor single-photon source. *Nano Lett.* **17**, 5446–5451 (2017).
32. Cai, T. et al. Coupling emission from single localized defects in two-dimensional semiconductor to surface plasmon polaritons. *Nano Lett.* **17**, 6564–6568 (2017).
33. Tran, T. T. et al. Deterministic coupling of quantum emitters in 2D materials to plasmonic nanocavity arrays. *Nano Lett.* **17**, 2634–2639 (2017).
34. Shimazaki, Y. et al. Strongly correlated electrons and hybrid excitons in a moiré heterostructure. *Nature* **580**, 472–477 (2020).
35. Zhong, D. et al. Van der Waals engineering of ferromagnetic semiconductor heterostructures for spin and valleytronics. *Sci. Adv.* **3**, e1603113 (2017).
36. Stern, H. L. et al. Room-temperature optically detected magnetic resonance of single defects in hexagonal boron nitride. *Nat. Commun.* **13**, 618 (2022).
37. Seifert, P. et al. Magic-angle bilayer graphene nanocalorimeters: toward broadband, energy-resolving single photon detection. *Nano Lett.* **20**, 3459–3464 (2020).
38. Tonndorf, P. et al. Single-photon emission from localized excitons in an atomically thin semiconductor. *Optica* **2**, 347–352 (2015).
39. Koperski, M. et al. Single photon emitters in exfoliated WSe_2 structures. *Nat. Nanotechnol.* **10**, 503–506 (2015).
40. Srivastava, A. et al. Optically active quantum dots in monolayer WSe_2. *Nat. Nanotechnol.* **10**, 491–496 (2015).
41. Chakraborty, C., Kinnischtzke, L., Goodfellow, K. M., Beams, R. & Vamivakas, A. N. Voltage-controlled quantum light from an atomically thin semiconductor. *Nat. Nanotechnol.* **10**, 507–511 (2015).
42. He, Y.-M. et al. Single quantum emitters in monolayer semiconductors. *Nat. Nanotechnol.* **10**, 497–502 (2015).
43. Palacios-Berraquero, C. et al. Atomically thin quantum light-emitting diodes. *Nat. Commun.* **7**, 12978 (2016).
44. Yu, L. et al. Site-controlled quantum emitters in monolayer $MoSe_2$. *Nano Lett.* **21**, 2376–2381 (2021).
45. Klein, J. et al. Site-selectively generated photon emitters in monolayer MoS_2 via local helium ion irradiation. *Nat. Commun.* **10**, 2755 (2019).
46. Zhao, H., Pettes, M. T., Zheng, Y. & Htoon, H. Site-controlled telecom-wavelength single-photon emitters in atomically-thin $MoTe_2$. *Nat. Commun.* **12**, 6753 (2021).
47. Tran, T. T., Bray, K., Ford, M. J., Toth, M. & Aharonovich, I. Quantum emission from hexagonal boron nitride monolayers. *Nat. Nanotechnol.* **11**, 37–41 (2016).
48. Montblanch, A. R.-P. et al. Confinement of long-lived interlayer excitons in WS_2/WSe_2 heterostructures. *Commun. Phys.* **4**, 119 (2021).
49. Kremser, M. et al. Discrete interactions between a few interlayer excitons trapped at a $MoSe_2$–WSe_2 heterointerface. *npj 2D Mater. Appl.* **4**, 8 (2020).
50. Zhaon, H. et al. Manipulating interlayer excitons for ultra-pure near-infrared quantum light generation. Preprint at https://arxiv.org/abs/2205.02472 (2022).
51. Wang, W. & Ma, X. Strain-induced trapping of indirect excitons in $MoSe_2/WSe_2$ heterostructures. *ACS Photon.* **7**, 2460–2467 (2020).
52. Baek, H. et al. Highly energy-tunable quantum light from moiré-trapped excitons. *Sci. Adv.* **6**, eaba8526 (2020).
53. Tonndorf, P. et al. Single-photon emitters in GaSe. *2D Mater.* **4**, 021010 (2017).
54. Mudd, G. W. et al. The direct-to-indirect band gap crossover in two-dimensional van der Waals indium selenide crystals. *Sci. Rep.* **6**, 39619 (2016).
55. Feuer, M. S. G. et al. Identification of exciton complexes in a charge-tunable Janus WSeS monolayer. *ACS Nano* **17**, 7326–7334 (2023).
56. Luo, Y., Liu, N., Li, X., Hone, J. C. & Strauf, S. Single photon emission in WSe_2 up 160 K by quantum yield control. *2D Mater.* **6**, 035017 (2019).
57. Parto, K., Azzam, S. I., Banerjee, K. & Moody, G. Defect and strain engineering of monolayer WSe_2 enables site-controlled single-photon emission up to 150 K. *Nat. Commun.* **12**, 3585 (2021).
58. Palacios-Berraquero, C. et al. Large-scale quantum-emitter arrays in atomically thin semiconductors. *Nat. Commun.* **8**, 15093 (2017).
59. Kumar, S. et al. Resonant laser spectroscopy of localized excitons in monolayer WSe_2. *Optica* **3**, 882–886 (2016).
60. Barbone, M. et al. Charge-tuneable biexciton complexes in monolayer WSe_2. *Nat. Commun.* **9**, 3721 (2018).
61. Mostaani, E. et al. Charge-carrier complexes in monolayer semiconductors. Preprint at https://arxiv.org/abs/2209.01593 (2022).
62. Branny, A., Kumar, S., Proux, R. & Gerardot, B. D. Deterministic strain-induced arrays of quantum emitters in a two-dimensional semiconductor. *Nat. Commun.* **8**, 15053 (2017).
63. Luo, Y. et al. Deterministic coupling of site-controlled quantum emitters in monolayer WSe_2 to plasmonic nanocavities. *Nat. Nanotechnol.* **13**, 1137–1142 (2018).
64. Rosenberger, M. R. et al. Quantum calligraphy: writing single-photon emitters in a two-dimensional materials platform. *ACS Nano* **13**, 904–912 (2019).
65. Flatten, L. C. et al. Microcavity enhanced single photon emission from two-dimensional WSe_2. *Appl. Phys. Lett.* **112**, 191105 (2018).
66. Iff, O. et al. Deterministic coupling of quantum emitters in WSe_2 monolayers to plasmonic nanocavities. *Opt. Express* **26**, 25944–25951 (2018).
67. Chakraborty, C. et al. Quantum-confined Stark effect of individual defects in a van der Waals heterostructure. *Nano Lett.* **17**, 2253–2258 (2017).
68. Kim, H., Moon, J. S., Noh, G., Lee, J. & Kim, J.-H. Position and frequency control of strain-induced quantum emitters in WSe_2 monolayers. *Nano Lett.* **19**, 7534–7539 (2019).

69. Iff, O. et al. Strain-tunable single photon sources in WSe_2 monolayers. *Nano Lett.* **19**, 6931–6936 (2019).
70. Lindlau, J. et al. The role of momentum-dark excitons in the elementary optical response of bilayer WSe_2. *Nat. Commun.* **9**, 2586 (2018).
71. Zhang, S. et al. Defect structure of localized excitons in a WSe_2 monolayer. *Phys. Rev. Lett.* **119**, 046101 (2017).
72. Linhart, L. et al. Localized intervalley defect excitons as single-photon emitters in WSe_2. *Phys. Rev. Lett.* **123**, 146401 (2019).
73. Xu, Y. et al. Creation of moiré bands in a monolayer semiconductor by spatially periodic dielectric screening. *Nat. Mater.* **20**, 645–649 (2021).
74. Moon, H. et al. Strain-correlated localized exciton energy in atomically thin semiconductors. *ACS Photon.* **7**, 1135–1140 (2020).
75. Darlington, T. P. et al. Imaging strain-localized excitons in nanoscale bubbles of monolayer WSe_2 at room temperature. *Nat. Nanotechnol.* **15**, 854–860 (2020).
76. Gelly, R. J. et al. Probing dark exciton navigation through a local strain landscape in a WSe_2 monolayer. *Nat. Commun.* **13**, 232 (2022).
77. Chakraborty, C., Goodfellow, K. M. & Vamivakas, A. N. Localized emission from defects in $MoSe_2$ layers. *Opt. Mater. Express* **6**, 2081–2087 (2016).
78. Branny, A. et al. Discrete quantum dot like emitters in monolayer $MoSe_2$: spatial mapping, magneto-optics, and charge tuning. *Appl. Phys. Lett.* **108**, 142101 (2016).
79. Wang, W., Jones, L. O., Chen, J.-S., Schatz, G. C. & Ma, X. Utilizing ultraviolet photons to generate single-photon emitters in semiconductor monolayers. *ACS Nano* **16**, 21240–21247 (2022).
80. Klein, J. et al. Engineering the luminescence and generation of individual defect emitters in atomically thin MoS_2. *ACS Photon.* **8**, 669–677 (2021).
81. Barthelmi, K. et al. Atomistic defects as single-photon emitters in atomically thin MoS_2. *Appl. Phys. Lett.* **117**, 070501 (2020).
82. Hötger, A. et al. Gate-switchable arrays of quantum light emitters in contacted monolayer MoS_2 van der Waals heterodevices. *Nano Lett.* **21**, 1040–1046 (2021).
83. Ye, Y. et al. Single photon emission from deep-level defects in monolayer WS_2. *Phys. Rev. B* **95**, 245313 (2017).
84. Daveau, R. S. et al. Spectral and spatial isolation of single tungsten diselenide quantum emitters using hexagonal boron nitride wrinkles. *APL Photon.* **5**, 096105 (2020).
85. Cadiz, F. et al. Excitonic linewidth approaching the homogeneous limit in MoS_2-based van der Waals heterostructures. *Phys. Rev. X* **7**, 021026 (2017).
86. Iff, O. et al. Substrate engineering for high-quality emission of free and localized excitons from atomic monolayers in hybrid architectures. *Optica* **4**, 669–673 (2017).
87. Abidi, I. H. et al. Selective defect formation in hexagonal boron nitride. *Adv. Opt. Mater.* **7**, 1900397 (2019).
88. Ngoc My Duong, H. et al. Effects of high-energy electron irradiation on quantum emitters in hexagonal boron nitride. *ACS Appl. Mater. Interfaces* **10**, 24886–24891 (2018).
89. Tawfik, S. A. et al. First-principles investigation of quantum emission from hBN defects. *Nanoscale* **9**, 13575–13582 (2017).
90. Gottscholl, A. et al. Initialization and read-out of intrinsic spin defects in a van der Waals crystal at room temperature. *Nat. Mater.* **19**, 540–545 (2020).
91. Meuret, S. et al. Photon bunching in cathodoluminescence. *Phys. Rev. Lett.* **114**, 197401 (2015).
92. Li, X. et al. Nonmagnetic quantum emitters in boron nitride with ultranarrow and sideband-free emission spectra. *ACS Nano* **11**, 6652–6660 (2017).
93. Hayee, F. et al. Revealing multiple classes of stable quantum emitters in hexagonal boron nitride with correlated optical and electron microscopy. *Nat. Mater.* **19**, 534–539 (2020).
94. Mendelson, N. et al. Identifying carbon as the source of visible single-photon emission from hexagonal boron nitride. *Nat. Mater.* **20**, 321–328 (2021).
95. Li, K., Smart, T. J. & Ping, Y. Carbon trimer as a 2 eV single-photon emitter candidate in hexagonal boron nitride: a first-principles study. *Phys. Rev. Mater.* **6**, L042201 (2022).
96. Golami, O. et al. Ab initio and group theoretical study of properties of a carbon trimer defect in hexagonal boron nitride. *Phys. Rev. B* **105**, 184101 (2022).
97. Tan, Q. et al. Donor–acceptor pair quantum emitters in hexagonal boron nitride. *Nano Lett.* **22**, 1331–1337 (2022).
98. Mendelson, N., Doherty, M., Toth, M., Aharonovich, I. & Tran, T. T. Strain-induced modification of the optical characteristics of quantum emitters in hexagonal boron nitride. *Adv. Mater.* **32**, 1908316 (2020).
99. Xia, Y. et al. Room-temperature giant Stark effect of single photon emitter in van der Waals material. *Nano Lett.* **19**, 7100–7105 (2019).
100. White, S. J. U. et al. Electrical control of quantum emitters in a Van der Waals heterostructure. *Light Sci. Appl.* **11**, 186 (2022).
101. Li, X., Scully, R. A., Shayan, K., Luo, Y. & Strauf, S. Near-unity light collection efficiency from quantum emitters in boron nitride by coupling to metallo-dielectric antennas. *ACS Nano* **13**, 6992–6997 (2019).
102. Vogl, T., Lecamwasam, R., Buchler, B. C., Lu, Y. & Lam, P. K. Compact cavity-enhanced single-photon generation with hexagonal boron nitride. *ACS Photon.* **6**, 1955–1962 (2019).
103. Fröch, J. E. et al. Coupling hexagonal boron nitride quantum emitters to photonic crystal cavities. *ACS Nano* **14**, 7085–7091 (2020).
104. Kim, S. et al. Photonic crystal cavities from hexagonal boron nitride. *Nat. Commun.* **9**, 2623 (2018).
105. Chejanovsky, N. et al. Single-spin resonance in a van der Waals embedded paramagnetic defect. *Nat. Mater.* **20**, 1079–1084 (2021).
106. Exarhos, A. L., Hopper, D. A., Patel, R. N., Doherty, M. W. & Bassett, L. C. Magnetic-field-dependent quantum emission in hexagonal boron nitride at room temperature. *Nat. Commun.* **10**, 222 (2019).
107. Rivera, P. et al. Interlayer valley excitons in heterobilayers of transition metal dichalcogenides. *Nat. Nanotechnol.* **13**, 1004–1015 (2018).
108. Karni, O. et al. Infrared interlayer exciton emission in MoS_2/WSe_2 heterostructures. *Phys. Rev. Lett.* **123**, 247402 (2019).
109. Zhang, Y. et al. Every-other-layer dipolar excitons in a spin–valley locked superlattice. *Nat. Nanotechnol.* https://doi.org/10.1038/s41565-023-01350-1 (2023).
110. Alexeev, E. M. et al. Resonantly hybridized excitons in moiré superlattices in van der Waals heterostructures. *Nature* **567**, 81–86 (2019).
111. Jin, C. et al. Observation of moiré excitons in WSe_2/WS_2 heterostructure superlattices. *Nature* **567**, 76–80 (2019).
112. Seyler, K. L. et al. Signatures of moiré-trapped valley excitons in $MoSe_2/WSe_2$ heterobilayers. *Nature* **567**, 66–70 (2019).
113. Tran, K. et al. Evidence for moiré excitons in van der Waals heterostructures. *Nature* **567**, 71–75 (2019).
114. Huang, D., Choi, J., Shih, C.-K. & Li, X. Excitons in semiconductor moiré superlattices. *Nat. Nanotechnol.* **17**, 227–238 (2022).
115. Yu, H., Liu, G.-B., Tang, J., Xu, X. & Yao, W. Moiré excitons: from programmable quantum emitter arrays to spin–orbit-coupled artificial lattices. *Sci. Adv.* **3**, e1701696 (2017).
116. Brotons-Gisbert, M. et al. Spin–layer locking of interlayer excitons trapped in moiré potentials. *Nat. Mater.* **19**, 630–636 (2020).

117. Li, F., Wei, W., Zhao, P., Huang, B. & Dai, Y. Electronic and optical properties of pristine and vertical and lateral heterostructures of Janus MoSSe and WSSe. *J. Phys. Chem. Lett.* **8**, 5959–5965 (2017).
118. Lu, A.-Y. et al. Janus monolayers of transition metal dichalcogenides. *Nat. Nanotechnol.* **12**, 744–749 (2017).
119. Qin, Y. et al. Reaching the excitonic limit in 2D Janus monolayers by in situ deterministic growth. *Adv. Mater.* **34**, 2106222 (2022).
120. Gan, Z. et al. Chemical vapor deposition of high-optical-quality large-area monolayer Janus transition metal dichalcogenides. *Adv. Mater.* **34**, 2205226 (2022).
121. Van Tuan, D. et al. Six-Body and Eight-Body Exciton States in Monolayer WSe_2. *Phys. Rev. Lett.* **129**, 076801 (2022).
122. Gao, T., v. Helversen, M., Anton-Solanas, C., Schneider, C. & Heindel, T. Atomically-thin single-photon sources for quantum communication. *npj 2D Mater. Appl.* **7**, 4 (2022).
123. So, J.-P. et al. Polarization control of deterministic single-photon emitters in monolayer WSe_2. *Nano Lett.* **21**, 1546–1554 (2021).
124. White, D. et al. Atomically-thin quantum dots integrated with lithium niobate photonic chips. *Opt. Mater. Express* **9**, 441–448 (2019).
125. Peyskens, F., Chakraborty, C., Muneeb, M., Van Thourhout, D. & Englund, D. Integration of single photon emitters in 2D layered materials with a silicon nitride photonic chip. *Nat. Commun.* **10**, 4435 (2019).
126. Kianinia, M. et al. Robust solid-state quantum system operating at 800 K. *ACS Photon.* **4**, 768–773 (2017).
127. Vogl, T. et al. Radiation tolerance of two-dimensional material-based devices for space applications. *Nat. Commun.* **10**, 1202 (2019).
128. Vogl, T., Knopf, H., Weissflog, M., Lam, P. K. & Eilenberger, F. Sensitive single-photon test of extended quantum theory with two-dimensional hexagonal boron nitride. *Phys. Rev. Res.* **3**, 013296 (2021).
129. Zeng, H. Z. J. et al. Integrated room temperature single-photon source for quantum key distribution. *Opt. Lett.* **47**, 1673–1676 (2022).
130. Samaner, Ç., Paçal, S., Mutlu, G., Uyanık, K. & Ates, S. Free-space quantum key distribution with single photons from defects in hexagonal boron nitride. *Adv. Quantum Technol.* **5**, 2200059 (2022).
131. Brotons-Gisbert, M. et al. Coulomb blockade in an atomically thin quantum dot coupled to a tunable Fermi reservoir. *Nat. Nanotechnol.* **14**, 442–446 (2019).
132. Mukherjee, A. et al. Observation of site-controlled localized charged excitons in CrI_3/WSe_2 heterostructures. *Nat. Commun.* **11**, 5502 (2020).
133. He, Y.-M. et al. Cascaded emission of single photons from the biexciton in monolayered WSe_2. *Nat. Commun.* **7**, 13409 (2016).
134. Young, R. J. et al. Entangled photons from the biexciton cascade of quantum dots. *J. Appl. Phys.* **101**, 081711 (2007).
135. Dey, P. et al. Gate-controlled spin–valley locking of resident carriers in WSe_2 monolayers. *Phys. Rev. Lett.* **119**, 137401 (2017).
136. Lu, X. et al. Optical initialization of a single spin–valley in charged WSe_2 quantum dots. *Nat. Nanotechnol.* **14**, 426–431 (2019).
137. Wang, Y. et al. Spin–valley locking effect in defect states of monolayer MoS_2. *Nano Lett.* **20**, 2129–2136 (2020).
138. Mirhosseini, M., Sipahigil, A., Kalaee, M. & Painter, O. Superconducting qubit to optical photon transduction. *Nature* **588**, 599–603 (2020).
139. Morell, N. et al. High quality factor mechanical resonators based on WSe_2 monolayers. *Nano Lett.* **16**, 5102–5108 (2016).
140. Xie, H. et al. Tunable exciton–optomechanical coupling in suspended monolayer $MoSe_2$. *Nano Lett.* **21**, 2538–2543 (2021).
141. Bereyhi, M. J. et al. Perimeter modes of nanomechanical resonators exhibit quality factors exceeding 10^9 at room temperature. *Phys. Rev. X* **12**, 021036 (2022).
142. Beccari, A. et al. Strained crystalline nanomechanical resonators with quality factors above 10 billion. *Nat. Phys.* **18**, 436–441 (2022).
143. Patel, S. D. et al. Surface acoustic wave cavity optomechanics with WSe_2 single photon emitters. Preprint at https://arxiv.org/abs/2211.15811 (2022).
144. Kolkowitz, S. et al. Coherent sensing of a mechanical resonator with a single-spin qubit. *Science* **335**, 1603–1606 (2012).
145. Marshall, W., Simon, C., Penrose, R. & Bouwmeester, D. Towards quantum superpositions of a mirror. *Phys. Rev. Lett.* **91**, 130401 (2003).
146. Marletto, C. & Vedral, V. Gravitationally induced entanglement between two massive particles is sufficient evidence of quantum effects in gravity. *Phys. Rev. Lett.* **119**, 240402 (2017).
147. Exarhos, A. L., Hopper, D. A., Grote, R. R., Alkauskas, A. & Bassett, L. C. Optical signatures of quantum emitters in suspended hexagonal boron nitride. *ACS Nano* **11**, 3328–3336 (2017).
148. Gottscholl, A. et al. Room temperature coherent control of spin defects in hexagonal boron nitride. *Sci. Adv.* **7**, eabf3630 (2021).
149. Gottscholl, A. et al. Spin defects in hBN as promising temperature, pressure and magnetic field quantum sensors. *Nat. Commun.* **12**, 4480 (2021).
150. Gao, X. et al. High-contrast plasmonic-enhanced shallow spin defects in hexagonal boron nitride for quantum sensing. *Nano Lett.* **21**, 7708–7714 (2021).
151. Dovzhenko, Y. et al. Magnetostatic twists in room-temperature skyrmions explored by nitrogen–vacancy center spin texture reconstruction. *Nat. Commun.* **9**, 2712 (2018).
152. Gross, I. et al. Real-space imaging of non-collinear antiferromagnetic order with a single-spin magnetometer. *Nature* **549**, 252–256 (2017).
153. Healey, A. J. et al. Quantum microscopy with van der Waals heterostructures. *Nat. Phys.* **19**, 87–91 (2023).
154. Mahdikhanysarvejahany, F. et al. Localized interlayer excitons in $MoSe_2$–WSe_2 heterostructures without a moiré potential. *Nat. Commun.* **13**, 5354 (2022).
155. Kennes, D. M. et al. Moiré heterostructures as a condensed-matter quantum simulator. *Nat. Phys.* **17**, 155–163 (2021).
156. Wang, X. et al. Light-induced ferromagnetism in moiré superlattices. *Nature* **604**, 468–473 (2022).
157. Husimi, K. & Syôzi, I. The statistics of honeycomb and triangular lattice. I. *Prog. Theor. Phys.* **5**, 177–186 (1950).
158. Kanamori, J. Electron correlation and ferromagnetism of transition metals. *Prog. Theor. Phys.* **30**, 275–289 (1963).
159. Sun, B. et al. Evidence for equilibrium exciton condensation in monolayer WTe_2. *Nat. Phys.* **18**, 94–99 (2022).
160. Lahaye, T., Menotti, C., Santos, L., Lewenstein, M. & Pfau, T. The physics of dipolar bosonic quantum gases. *Rep. Prog. Phys.* **72**, 126401 (2009).
161. Yagmurcukardes, M. et al. Quantum properties and applications of 2D Janus crystals and their superlattices. *Appl. Phys. Rev.* **7**, 011311 (2020).
162. Riis-Jensen, A. C., Pandey, M. & Thygesen, K. S. Efficient charge separation in 2D Janus van der Waals structures with built-in electric fields and intrinsic p–n doping. *J. Phys. Chem. C.* **122**, 24520–24526 (2018).
163. Jauregui, L. A. et al. Electrical control of interlayer exciton dynamics in atomically thin heterostructures. *Science* **366**, 870–875 (2019).
164. Guo, H., Zhang, X. & Lu, G. Tuning moiré excitons in Janus heterobilayers for high-temperature Bose–Einstein condensation. *Sci. Adv.* **8**, eabp9757 (2022).
165. Zhang, Z. et al. Endoepitaxial growth of monolayer mosaic heterostructures. *Nat. Nanotechnol.* **17**, 493–499 (2022).

166. Guo, Y. et al. Designing artificial two-dimensional landscapes via atomic-layer substitution. *Proc. Natl Acad. Sci. USA* **118**, e2106124118 (2021).
167. Gisin, N., Ribordy, G., Tittel, W. & Zbinden, H. Quantum cryptography. *Rev. Mod. Phys.* **74**, 145–195 (2002).
168. Hadfield, R. H. Single-photon detectors for optical quantum information applications. *Nat. Photon.* **3**, 696–705 (2009).
169. Varnava, M., Browne, D. E. & Rudolph, T. How good must single photon sources and detectors be for efficient linear optical quantum computation? *Phys. Rev. Lett.* **100**, 060502 (2008).
170. Cheng, R. et al. Broadband on-chip single-photon spectrometer. *Nat. Commun.* **10**, 4104 (2019).
171. Cao, Y. et al. Unconventional superconductivity in magic-angle graphene superlattices. *Nature* **556**, 43–50 (2018).
172. Cao, Y. et al. Quality heterostructures from two-dimensional crystals unstable in air by their assembly in inert atmosphere. *Nano Lett.* **15**, 4914–4921 (2015).
173. Orchin, G. J. et al. Niobium diselenide superconducting photodetectors. *Appl. Phys. Lett.* **114**, 251103 (2019).
174. Seifert, P. et al. A high-T_c van der Waals superconductor based photodetector with ultra-high responsivity and nanosecond relaxation time. *2D Mater.* **8**, 035053 (2021).
175. Lee, G.-H. et al. Graphene-based Josephson junction microwave bolometer. *Nature* **586**, 42–46 (2020).
176. Walsh, E. D. et al. Josephson junction infrared single-photon detector. *Science* **372**, 409–412 (2021).
177. Zhang, S. et al. Nano-spectroscopy of excitons in atomically thin transition metal dichalcogenides. *Nat. Commun.* **13**, 542 (2022).
178. Avdeev, I. D. & Smirnov, D. S. Hyperfine interaction in atomically thin transition metal dichalcogenides. *Nanoscale Adv.* **1**, 2624–2632 (2019).
179. Winter, M. Molybdenum: isotope data. *WebElements* http://www.webelements.com/molybdenum/isotopes.html (2023).
180. Fanciulli, M. Electron paramagnetic resonance and relaxation in BN and BN:C. *Philos. Mag. B* **76**, 363–381 (1997).
181. Katzir, A., Suss, J. T., Zunger, A. & Halperin, A. Point defects in hexagonal boron nitride. EPR, thermoluminescence, and thermally-stimulated-current measurements. *Phys. Rev. B* **11**, 2370–2377 (1975).
182. Murzakhanov, F. F. et al. Electron–nuclear coherent coupling and nuclear spin readout through optically polarized V_B^- spin states in hBN. *Nano Lett.* **22**, 2718–2724 (2022).
183. Gao, X. et al. Nuclear spin polarization and control in hexagonal boron nitride. *Nat. Mater.* **21**, 1024–1028 (2022).
184. Pompili, M. et al. Realization of a multinode quantum network of remote solid-state qubits. *Science* **372**, 259–264 (2021).
185. Hermans, S. L. N. et al. Qubit teleportation between non-neighbouring nodes in a quantum network. *Nature* **605**, 663–668 (2022).
186. Hermans, S. L. N. et al. Entangling remote qubits using the single-photon protocol: an in-depth theoretical and experimental study. *New J. Phys.* **25**, 013011 (2023).
187. Michaels, C. P. et al. Multidimensional cluster states using a single spin–photon interface coupled strongly to an intrinsic nuclear register. *Quantum* **5**, 565 (2021).
188. Raussendorf, R., Browne, D. E. & Briegel, H. J. Measurement-based quantum computation on cluster states. *Phys. Rev. A* **68**, 022312 (2003).
189. Song, T. et al. Direct visualization of magnetic domains and moiré magnetism in twisted 2D magnets. *Science* **374**, 1140–1144 (2021).
190. Li, W. et al. Local sensing of correlated electrons in dual-moiré heterostructures using dipolar excitons. Preprint at https://arxiv.org/abs/2111.09440 (2021).
191. Ma, L. et al. Strongly correlated excitonic insulator in atomic double layers. *Nature* **598**, 585–589 (2021).
192. Bai, Y. et al. Excitons in strain-induced one-dimensional moiré potentials at transition metal dichalcogenide heterojunctions. *Nat. Mater.* **19**, 1068–1073 (2020).
193. Dirnberger, F. et al. Quasi-1D exciton channels in strain-engineered 2D materials. *Sci. Adv.* **7**, eabj3066 (2021).
194. Sahoo, P. K., Memaran, S., Xin, Y., Balicas, L. & Gutiérrez, H. R. One-pot growth of two-dimensional lateral heterostructures via sequential edge-epitaxy. *Nature* **553**, 63–67 (2018).
195. Voiry, D., Mohite, A. & Chhowalla, M. Phase engineering of transition metal dichalcogenides. *Chem. Soc. Rev.* **44**, 2702–2712 (2015).
196. Stefan, L. et al. Multiangle reconstruction of domain morphology with all-optical diamond magnetometry. *Phys. Rev. Appl.* **16**, 014054 (2021).
197. Errando-Herranz, C. et al. Resonance fluorescence from waveguide-coupled, strain-localized, two-dimensional quantum emitters. *ACS Photon.* **8**, 1069–1076 (2021).
198. Xu, Y. et al. Correlated insulating states at fractional fillings of moiré superlattices. *Nature* **587**, 214–218 (2020).
199. Santori, C., Fattal, D., Vučković, J., Solomon, G. S. & Yamamoto, Y. Indistinguishable photons from a single-photon device. *Nature* **419**, 594–597 (2002).
200. Balasubramanian, G. et al. Nanoscale imaging magnetometry with diamond spins under ambient conditions. *Nature* **455**, 648–651 (2008).
201. Somaschi, N. et al. Near-optimal single-photon sources in the solid state. *Nat. Photon.* **10**, 340–345 (2016).
202. Healey, A. J. et al. Quantum microscopy with van der Waals heterostructures. *Nat. Phys.* **19**, 87–91 (2023).
203. Kalb, N. et al. Entanglement distillation between solid-state quantum network nodes. *Science* **356**, 928–932 (2017).
204. Nielsen, M. A. & Chuang, I. L. *Quantum Computation and Quantum Information* (Cambridge Univ. Press, 2000).
205. Blatt, R. & Roos, C. F. Quantum simulations with trapped ions. *Nat. Phys.* **8**, 277–284 (2012).
206. Wang, D. et al. Turning a molecule into a coherent two-level quantum system. *Nat. Phys.* **15**, 483–489 (2019).
207. Magnard, P. et al. Microwave quantum link between superconducting circuits housed in spatially separated cryogenic systems. *Phys. Rev. Lett.* **125**, 260502 (2020).
208. Senellart, P., Solomon, G. & White, A. High-performance semiconductor quantum-dot single-photon sources. *Nat. Nanotechnol.* **12**, 1026–1039 (2017).
209. Hahn, E. L. Spin echoes. *Phys. Rev.* **80**, 580–594 (1950).

Acknowledgements

We thank H. Beukers, J. M. Brevoord, A. Das, D. De Fazio, M. del Castillo, N. Demetriou, M. Feuer, R. Flaschmann, D. Gangloff, A. Gio-Pardo, M. Gündogan, S. Hermans, M. Iuliano, J. Jozan-Baldovinos, D. M. Kara, J. Klein, J. Knörzer, S. Loenen, C. Martínez, S. Marzban, A. Mortadelo-Filemón, K. Müller, B. Panh, M. Pasini, M. Petric, B. Pingault, N. Shofer, T. Simmet, L. Stefan, G. van de Stolpe, H. B. van Ommen and A. Kok Cheng Tan for useful discussions. We acknowledge funding from ERC grants Hetero2D, GSYNCOR and GIPT, EPSRC grants EP/K01711X/1, EP/K017144/1, EP/N010345/1, EP/L016087/1, EP/X015742/1, and EP/V000055/1, EU Graphene and Quantum Flagships, EU grants CHARM and Graph-X, the Alexander von Humboldt Foundation, the Australian Research Council (CE200100010, FT220100053) and the Office of Naval Research Global (N62909-22-1-2028).

Competing interests

The authors declare no competing interests.

Additional information

Supplementary information The online version contains supplementary material available at https://doi.org/10.1038/s41565-023-01354-x.

Correspondence and requests for materials should be addressed to Mete Atatüre or Andrea C. Ferrari.

Peer review information *Nature Nanotechnology* thanks Kuan Eng Johnson Goh and the other, anonymous, reviewer(s) for their contribution to the peer review of this work.